

REPORT DOCUMENTATION PAGE				Form Approved OMB No. 0704-0188	
The public reporting burden for this collection of information is estimated to average 1 hour per response, including the time for reviewing instructions, searching existing data sources, gathering and maintaining the data needed, and completing and reviewing the collection of information. Send comments regarding this burden estimate or any other aspect of this collection of information, including suggestions for reducing the burden, to the Department of Defense, Executive Service Directorate (0704-0188). Respondents should be aware that notwithstanding any other provision of law, no person shall be subject to any penalty for failing to comply with a collection of information if it does not display a currently valid OMB control number.					
<b>PLEASE DO NOT RETURN YOUR FORM TO THE ABOVE ORGANIZATION.</b>					
<b>1. REPORT DATE (DD-MM-YYYY)</b> 14 July 20		<b>2. REPORT TYPE</b> <i>Final Report</i>		<b>3. DATES COVERED (From - To)</b> 13 Nov 2007-11 Nov 2009	
<b>4. TITLE AND SUBTITLE</b> STTR (PHASE II) Stability models for augment design tools and technology assessment			<b>5a. CONTRACT NUMBER</b> FA9550-08-C-0039		
			<b>5b. GRANT NUMBER</b>		
			<b>5c. PROGRAM ELEMENT NUMBER</b> 65502F		
			<b>5d. PROJECT NUMBER</b> STTR		
<b>6. AUTHOR(S)</b> Pro, Godfrey Mungal Stanford University			<b>5e. TASK NUMBER</b> TX		
			<b>5f. WORK UNIT NUMBER</b>		
			<b>8. PERFORMING ORGANIZATION REPORT NUMBER</b>		
<b>7. PERFORMING ORGANIZATION NAME(S) AND ADDRESS(ES)</b> Stanford University Stanford, California 94308			<b>10. SPONSOR/MONITOR'S ACRONYM(S)</b>  <b>11. SPONSOR/MONITOR'S REPORT NUMBER(S)</b> AFRL-OSR-VA-TR-2013-1014		
<b>9. SPONSORING/MONITORING AGENCY NAME(S) AND ADDRESS(ES)</b> Air Force Office of Scientific Research 875 N Randolph Street Arlington, VA 22203					
<b>12. DISTRIBUTION/AVAILABILITY STATEMENT</b> Distribution A: Approved for public release. Distribution is unlimited					
<b>13. SUPPLEMENTARY NOTES</b>					
<b>14. ABSTRACT</b> The overall objective of the project is to computationally and experimentally design and study new flame stabilizers for augmentor systems that lead to an improved static flame stability. The main objectives of the project are: 1) development of various newly designed bluff body bases, 2) experimental investigation of static flame stability with the various prototype base geometries and 3) demonstration of numerical predictions of the experiments. In accordance with these objectives, the experimental studies have focused on proposing local cavity based base geometries and investigating their effect on liftoff heights and blowout limits under the following flame configurations: 1) partially premixed flame in an high temperature vitiated flow, 2) a partially premixed flame in the room temperature air flow and 3) a fully premixed flame and 4) a hybrid fully and partially premixed flames.					
<b>15. SUBJECT TERMS</b> Computational, geometries, prototype, premixed, flame and hybrid, augmentor, turbulent combustion					
<b>16. SECURITY CLASSIFICATION OF:</b>			<b>17. LIMITATION OF ABSTRACT</b>  UL	<b>18. NUMBER OF PAGES</b>	<b>19a. NAME OF RESPONSIBLE PERSON</b> Julian Tishkoff
<b>a. REPORT</b> Unclassified	<b>b. ABSTRACT</b> Unclassified	<b>c. THIS PAGE</b> Unclassified			<b>19b. TELEPHONE NUMBER (Include area code)</b> 703-696-8478

## INSTRUCTIONS FOR COMPLETING SF 298

**1. REPORT DATE.** Full publication date, including day, month, if available. Must cite at least the year and be Year 2000 compliant, e.g. 30-06-1998; xx-06-1998; xx-xx-1998.

**2. REPORT TYPE.** State the type of report, such as final, technical, interim, memorandum, master's thesis, progress, quarterly, research, special, group study, etc.

**3. DATES COVERED.** Indicate the time during which the work was performed and the report was written, e.g., Jun 1997 - Jun 1998; 1-10 Jun 1996; May - Nov 1998; Nov 1998.

**4. TITLE.** Enter title and subtitle with volume number and part number, if applicable. On classified documents, enter the title classification in parentheses.

**5a. CONTRACT NUMBER.** Enter all contract numbers as they appear in the report, e.g. F33615-86-C-5169.

**5b. GRANT NUMBER.** Enter all grant numbers as they appear in the report, e.g. AFOSR-82-1234.

**5c. PROGRAM ELEMENT NUMBER.** Enter all program element numbers as they appear in the report, e.g. 61101A.

**5d. PROJECT NUMBER.** Enter all project numbers as they appear in the report, e.g. 1F665702D1257; ILIR.

**5e. TASK NUMBER.** Enter all task numbers as they appear in the report, e.g. 05; RF0330201; T4112.

**5f. WORK UNIT NUMBER.** Enter all work unit numbers as they appear in the report, e.g. 001; AFAPL30480105.

**6. AUTHOR(S).** Enter name(s) of person(s) responsible for writing the report, performing the research, or credited with the content of the report. The form of entry is the last name, first name, middle initial, and additional qualifiers separated by commas, e.g. Smith, Richard, J, Jr.

**7. PERFORMING ORGANIZATION NAME(S) AND ADDRESS(ES).** Self-explanatory.

**8. PERFORMING ORGANIZATION REPORT NUMBER.** Enter all unique alphanumeric report numbers assigned by the performing organization, e.g. BRL-1234; AFWL-TR-85-4017-Vol-21-PT-2.

**9. SPONSORING/MONITORING AGENCY NAME(S) AND ADDRESS(ES).** Enter the name and address of the organization(s) financially responsible for and monitoring the work.

**10. SPONSOR/MONITOR'S ACRONYM(S).** Enter, if available, e.g. BRL, ARDEC, NADC.

**11. SPONSOR/MONITOR'S REPORT NUMBER(S).** Enter report number as assigned by the sponsoring/monitoring agency, if available, e.g. BRL-TR-829; -215.

**12. DISTRIBUTION/AVAILABILITY STATEMENT.** Use agency-mandated availability statements to indicate the public availability or distribution limitations of the report. If additional limitations/ restrictions or special markings are indicated, follow agency authorization procedures, e.g. RD/FRD, PROPIN, ITAR, etc. Include copyright information.

**13. SUPPLEMENTARY NOTES.** Enter information not included elsewhere such as: prepared in cooperation with; translation of; report supersedes; old edition number, etc.

**14. ABSTRACT.** A brief (approximately 200 words) factual summary of the most significant information.

**15. SUBJECT TERMS.** Key words or phrases identifying major concepts in the report.

**16. SECURITY CLASSIFICATION.** Enter security classification in accordance with security classification regulations, e.g. U, C, S, etc. If this form contains classified information, stamp classification level on the top and bottom of this page.

**17. LIMITATION OF ABSTRACT.** This block must be completed to assign a distribution limitation to the abstract. Enter UU (Unclassified Unlimited) or SAR (Same as Report). An entry in this block is necessary if the abstract is to be limited.

**AF06-T033:**  
**Stability Models for Augmentor Design Tools and  
Technology Assessment**

Contractor:  
Cascade Technologies, Inc.  
1330 Charleston Road  
Mountain View, CA 94043

Contract number:  
FA9550-08-C-0039

*Principal Investigators:*

Dr. Shoreh Hajiloo  
Cascade Technologies, Inc.

Prof. Godgrey Mungal  
Stanford University.

Reporting period:  
11/13/07 - 11/12/08

## Contents

1	Summary	3
2	Objectives	4
3	Status of Effort	5
4	Accomplishments	5
4.1	Experimental Study	6
4.1.1	Modifications to the Bluff-Body Fuel Injection System	6
4.1.2	Implementation of Water Cooled Grid and Turbulence Grid	6
4.1.3	Effect of OH Radical Addition Through Hydrogen Peroxide ( $H_2O_2$ ) Injection	9
4.2	Modeling and Computation	12
4.2.1	Validation and Damköhler Number Similarity	12
	Numerical Formulation	13
	Flamelet Progress Variable Approach	14
	Non-Dimensional Governing Equations	15
	Damköhler Number Similarity	18
	Numerical Setup	21
	Results	21
	Conclusion	26
4.2.2	Large-Eddy Simulations of AFRL Flame Holder Experiment	29
	Flow Conditions	29
	Structured Flow Solver Cold Flow Results	29
	Structured Flow Solver Reactive Flow Results	29
	CharLES Low Mach Formulation Cold Flow Results	34
	2D Unsteady RANS Cold Flow Results	34
5	Personnel supported	43
6	Publications	43
7	Interactions/Transitions	43
8	New discoveries, inventions, or patent disclosures	44
9	Honors/Awards	44

## 1 Summary

The present project is aimed at developing validated models for predictions of static stability of combustion in augmentor systems, and further at the design of novel flame holding concepts. In the present reporting period, we performed large-eddy simulations of the Stanford vitiated flow experiment. We also proposed and computationally tested the concept of Damköhler number similarity for assessing flame stability in low speed experimental facilities. We further acquired a V-gutter geometry and the geometry of the new AFRL flame holder test facility and performed cold flow and reactive simulations of a specified flow condition as a first point of a flame stability map.

The experimental work has focused on improving the performance of the bluff-body augmentor system in preparation for detailed combustion studies. Improvements consist of modifications to the bluff-body fuel injection system and the implementation of a turbulence grid. We have also investigated the injection of hydrogen peroxide ( $\text{H}_2\text{O}_2$ ) in the post combustion stream. The use of a grid with higher turbulence conditions is used as a proxy for higher speed flow, while the use of hydrogen peroxide is used to study the effect of OH radical concentration on flame stability. The work described here has been conducted by post doctoral researcher Woogyung Kim with assistance from graduate students Hyungrok Do and Seong-kyun Im under the supervision of Prof. Godfrey Mungal. Details of the efforts are provided below.

## 2 Objectives

The overall objective of the project is to develop well tested and validated models that can predict processes for static stability in augmentor systems leading to a better design of advanced, compact, stable, and efficient augmentors. The emphasis of the proposed phase II work is to study, fundamentally understand, and model the chemical effect of vitiation on static stability in augmentor systems with computational and experimental methods, and to enhance and validate the predictive capabilities of the commercial multi-physics, unstructured large-eddy simulation code CharLES distributed by CASCADE Technologies. We will also propose and investigate new flame holder designs with improved static stability.

The project focusses mainly on three different fundamental aspects:

- Task 1: Investigation of the effects of vitiated oxidizer flow composition on flame stabilization. Experiments are carried out in the Stanford experimental rig to study flame stabilization in vitiated air. Different additives to the vitiated flow are considered to study the effects of several species, including OH, NO, and NO<sub>2</sub>, in more detail. The experimentally investigated flows are also computed with LES.
- Task 2: Computational model extension to consider mixed-mode augmentor stabilization and model validation. Model extensions that allow for a more accurate consideration of finite rate chemistry are being developed. Specifically, a model will be developed that can predict auto-ignition in turbulent environments, partially premixed turbulent combustion, non-premixed turbulent combustion, and the transition between the three regimes. All model developments will be validated using the data from our own experiments and from the AFRL HIT experiments.
- Task 3: Conceptual design of new augmentor flame holder with improved static stability. We will work on the conceptual design of new augmentor flame holders and test promising concepts in the Stanford experimental facility and at AFRL. The Damköhler number similarity will be demonstrated first. Pre-design of new flame holding concepts will then be developed in the Stanford vitiated flow experiment. The designs will finally be tested and further refined in the AFRL ASTAR experimental facility.

There is essentially no change from the originally proposed work. However, we propose a shift of emphasis to a closer collaboration with the newly planned AFRL experiments. This requires more emphasis on simulations of the AFRL data and less on simulations of the Stanford experiments than originally planned. We have now a more concrete plan for the augmentor design and model validation that was worked out in close collaborations with Dr. Kiel from AFRL. We will first validate the models with the Stanford low speed rig and the AFRL high speed rig, specifically using the new AFRL data that is presently being acquired. We are presently computing stability maps of the AFRL configuration, for which experiments will be done in the near future. The newly proposed flame holder designs will also be assessed in close

collaboration with AFRL. New geometries will first be assessed computationally and potential design changes will be performed. The design will then be tested in the Stanford low speed rig and the AFRL high speed facility. The test conditions will be chosen using the concept of Damköhler number similarity that is described in the present report. This will test both the predictive capability of the models, but also the predictiveness of the concept of Damköhler number similarity that is proposed in the present report.

### 3 Status of Effort

The present project is aimed at developing validated models for predictions of static stability of combustion in augmentor systems, and further at the design of novel flame holding concepts. In the present reporting period, we performed large-eddy simulations of the Stanford vitiated flow experiment. We also proposed and computationally tested the concept of Damköhler number similarity for assessing flame stability in low speed experimental facilities. We further acquired a V-gutter geometry and the geometry of the new AFRL flame holder test facility and performed cold flow and reactive simulations of a specified flow condition as a first point of a flame stability map. The experimental work has focused on improving the performance of the bluff-body augmentor system in preparation for detailed combustion studies. Improvements consist of modifications to the bluff-body fuel injection system and the implementation of a turbulence grid. We have also investigated the injection of hydrogen peroxide ( $\text{H}_2\text{O}_2$ ) in the post combustion stream. The use of a grid with higher turbulence conditions is used as a proxy for higher speed flow, while the use of hydrogen peroxide is used to study the effect of OH radical concentration on flame stability.

### 4 Accomplishments

In the present reporting period, we have worked on all tasks described above. In the experimental part, we have made significant modifications to the experimental facility to make the flow more homogeneous and more relevant to realistic augmentor systems. Data has been acquired in the new facility for validation and for assessing the influence of individual species in the vitiated stream. In the computational and modeling part of the project, we have performed validation simulations of the Stanford experiment. We have then used this case to propose and demonstrate the concept of Damköhler number similarity. Finally, we have acquired the geometry of the new AFRL high speed test rig, and we have performed several non-reactive and reactive simulations to compare reactive versus non-reactive flow and LES versus 2D RANS simulations. These accomplishments are presented in the following.

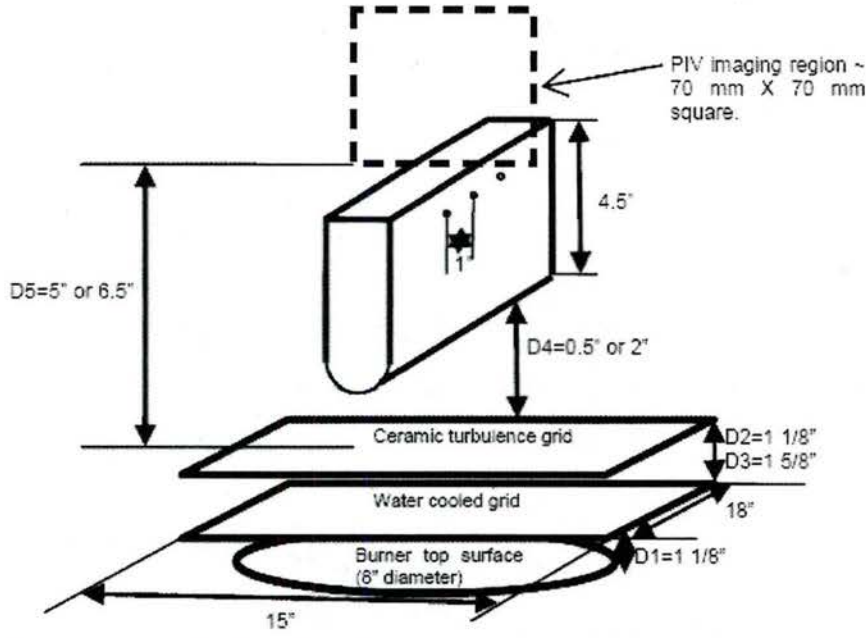
## 4.1 Experimental Study

### 4.1.1 Modifications to the Bluff-Body Fuel Injection System

The overall geometry of the bluff body is unchanged from that of Phase I, but the number of fuel injection holes on its sides has been adjusted from two centrally located holes in Phase I to ten holes, then finally settled onto a six hole configuration. The primary aims of these modifications are to increase the two dimensional symmetry of flames and to improve uniformity of the fuel flow. In the original two-hole case, the fuel flow was under a significant end boundary condition effect from the post combustion stream since only one fuel hole in each side of the bluff body existed. Two-dimensional symmetry from the configuration, therefore, was not achievable. When the number of holes was increased to ten (five on each side), it was found that the flame uniformity from each hole was problematic due to a pressure gradient along the 1/4" fuel delivery pipe; this was alleviated significantly if we used only six holes. Thus, the final 6 hole configuration obtained by deleting 4 holes at the boundaries from the 10 hole configuration satisfactorily provided both the two dimensional symmetry in the central region of the bluff body and good flame uniformity. All experiments described here, therefore, have been carried out using the 6 hole configuration.

### 4.1.2 Implementation of Water Cooled Grid and Turbulence Grid

The overall experimental setup with a newly added (from the setup of Phase I) water-cooled grid and a turbulence grid is provided in figure 1. While the main burner is unchanged from Phase I, the water-cooled copper grid which has a similar geometry to the condenser of a refrigerator is placed on the top of the main burner. The use of the water cooled grid eliminates the need for additional air/nitrogen injection into the post combustion gas (as used throughout Phase I), which added to the non-uniformity of the velocity and concentration fields of the post combustion stream. The turbulence grid is placed  $\sim 1''$  downstream of the top surface of the water-cooled grid (see Fig. 1 for detailed dimensions). Two opening spacings of the grid (25% and 36% opening areas) and two distances between the turbulence grid and the bluff body, 0.5" and 2", have been tested to optimize the level of turbulence. The detailed geometries of the water cooled grid and the turbulence grid are shown in Figs. 2(a) and 2(b), respectively. Water at room temperature flows through a 1/4" (OD), serpentine-shaped copper tube which has 11 turns within a 15" by 18" rectangular region. Numerous 1/16" (OD) copper wires are welded on the copper tube to improve heat conduction along the streamwise direction of water flow. The resulting temperature profile along the tube, therefore, can be more uniform. The turbulence grid (see Fig. 2(b)) is composed of two, top and bottom, layers of 1/2" OD, 8" long ceramic (99.9% Al<sub>2</sub>O<sub>3</sub>) tube arrays. Each array is formed by 6, 7, or 8 parallel-placed ceramic tubes, which depends on the size of opening areas (7 for top layer of 25 % opening; 8 for bottom layer of 25 % opening; and 6 for top and bottom layers of 36 % opening). The top and bottom arrays are placed perpendicular to each other such that the shape of the open area becomes square.



- D1: distance from the burner top surface to the center of water grid (1 1/8")  
D2: distance from the center of water grid to the center of bottom ceramic pipe array (1 1/8")  
D3: distance from the center of water grid to the center of top ceramic pipe array (1 5/8")

Figure 1: Schematic of overall experimental setup

The distances between the centers of adjacent tubes are 0" (25 % opening) and 1.25" (36 % opening), respectively.

Figure 3 shows sample PIV results to compare the turbulent kinetic energy,  $\frac{1}{2}(u'^2 + v'^2)$ , where  $u$  is the horizontal and  $v$  is the vertical velocity component, respectively, for three different cases: Without the turbulence grid (Fig. 3a), with the turbulence grids with 25 % opening area (Fig. 3b) and 36 % opening area (Fig. 3c). For all cases shown in Fig. 3, 50 individual images are ensemble-averaged and the water cooled grid is always implemented. Color coding of each figure represents the intensity of the turbulent kinetic energy (high turbulent kinetic energy in dark red regions and low in dark blue regions). In all three cases, initial flow conditions ( $\sim 0.65$  equivalence ratio in the inlet of the main burner,  $\sim 3.5$  m/s free stream speed,  $\sim 1200$  K free stream temperature, no bluff body) and imaging region ( $\sim 70$  mm x  $70$  mm square whose bottom line is located at  $5''$  above the top surface of the turbulence grid) are identical. As shown, the no-grid case has average turbulent kinetic energy of  $\sim 0.1$  (m/s)<sup>2</sup> (or  $u_{norm} \approx (u^2 + v^2)^{0.5} / v_{freestream} = 13\%$ ) while 25% and 36% opening cases have  $\sim 0.17$  m/s<sup>2</sup> and  $\sim 0.22$  m/s<sup>2</sup>, respectively (or  $u_{norm} \approx 17\%$  and  $\sim 19\%$ , respectively). Therefore, one can conclude that the 36 % opening area grid has a higher capability in generating more intense turbulence

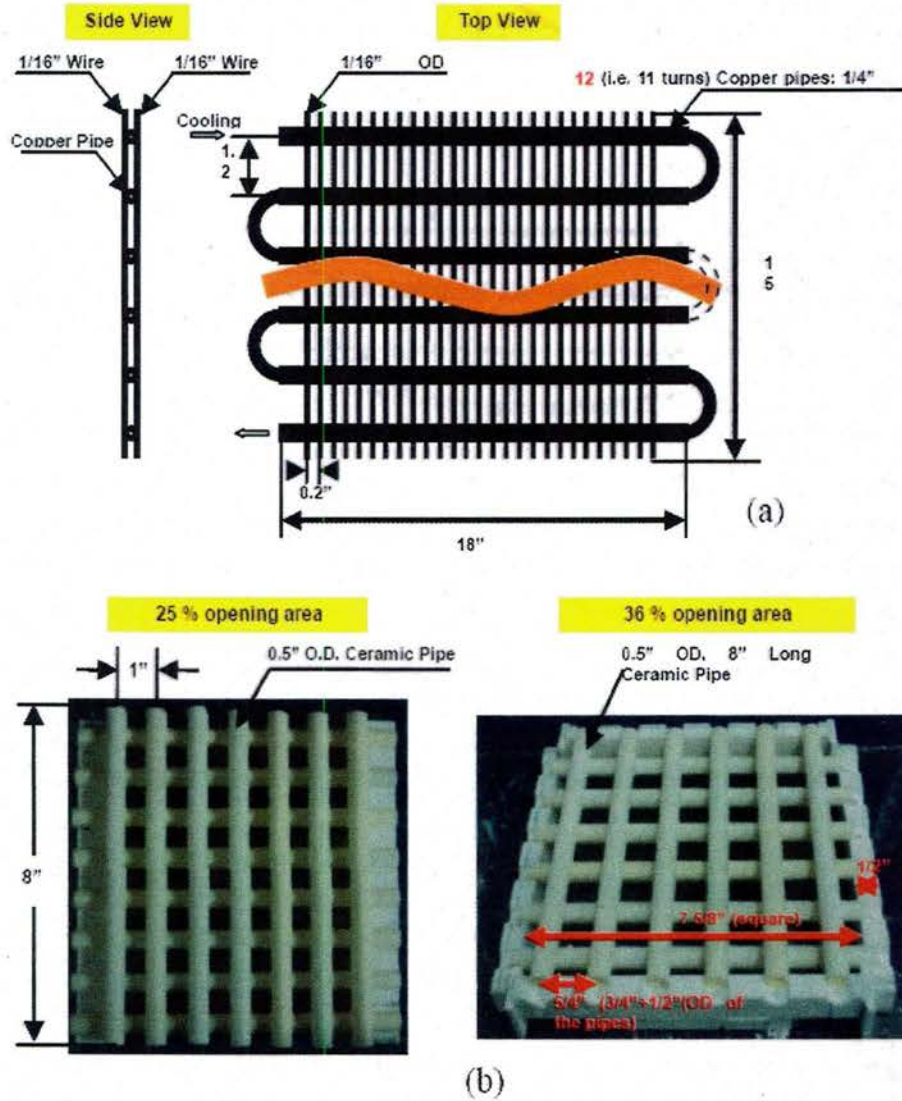


Figure 2: Detailed dimensions of (a) water cooled and (b) turbulence grids

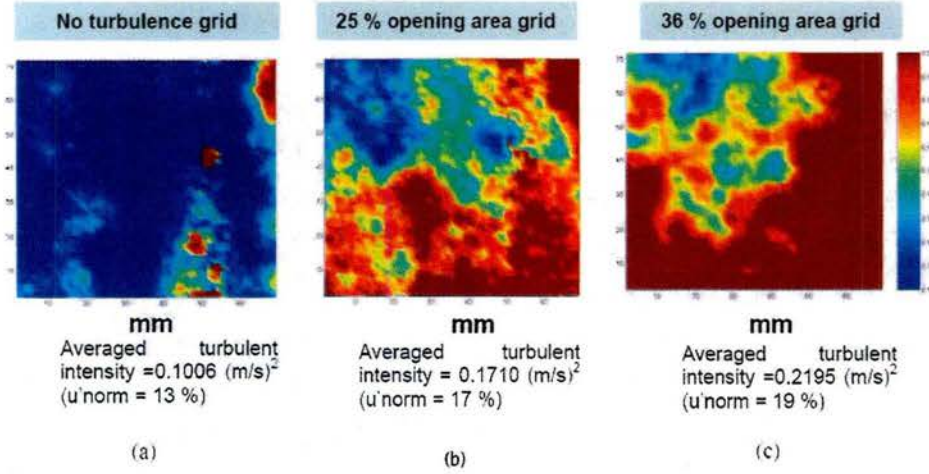


Figure 3: Turbulence intensities in the presence of (a) no grid, (b) 25 % opening area grid and (c) 36 % opening area grid

than the 25 % opening area grid.

Other sample PIV results obtained in the presence of the bluff body are shown in Fig. 4. Figures 4a and 4b show the results in the absence and presence of the turbulence grid (36 % opening area), respectively. Initial flow conditions are identical with those of Fig. 3, but the PIV imaging region is adjusted to 1.5" higher than that of Fig. 3 to investigate the possible decay of turbulence intensities further downstream than the case of Fig. 3. While the wake region due to the presence of the bluff body is well captured by the dark red region in both figures, one can observe that the case with the turbulence grid (Fig. 4b) still has higher freestream turbulence intensities ( $u_{norm} = \sim 23 \%$ ) than that without the grid ( $u_{norm} = \sim 19 \%$ ).

#### 4.1.3 Effect of OH Radical Addition Though Hydrogen Peroxide ( $H_2O_2$ ) Injection

The injection of  $H_2O_2$  into the post combustion gas is carried out with the setup shown in Fig. 5. The steady flow of liquid  $H_2O_2/H_2O$  solution (pure water, 30 vol.% or 50 vol.%  $H_2O_2$  solution in water) is implemented by a step motor/syringe assembly placed  $\sim 2$  m upstream of the main burner, while the liquid flows through four  $1/8''$  OD, 2 m long teflon tubes which connect the syringe and four central tubes in the top array of the turbulence grid. The total flowrate of the  $H_2O_2/H_2O$  solution provided by the step motor/syringe assembly is  $\sim 20$  sccm (liquid) for each experiment. The solution is in liquid phase until it reaches the inlets of the ceramic tubes, but is rapidly vaporized when it flows through the inside of the ceramic tubes. The resulting  $H_2O_2/H_2O$  vapor is injected into the post combustion gas through five  $\sim 1/8'' \times 1/16''$  rectangular shaped slits in each of the four ceramic tubes. The inter-spacing between adjacent holes on one ceramic tube is  $1''$ . Flame stabilities with the  $H_2O_2/H_2O$  injection are

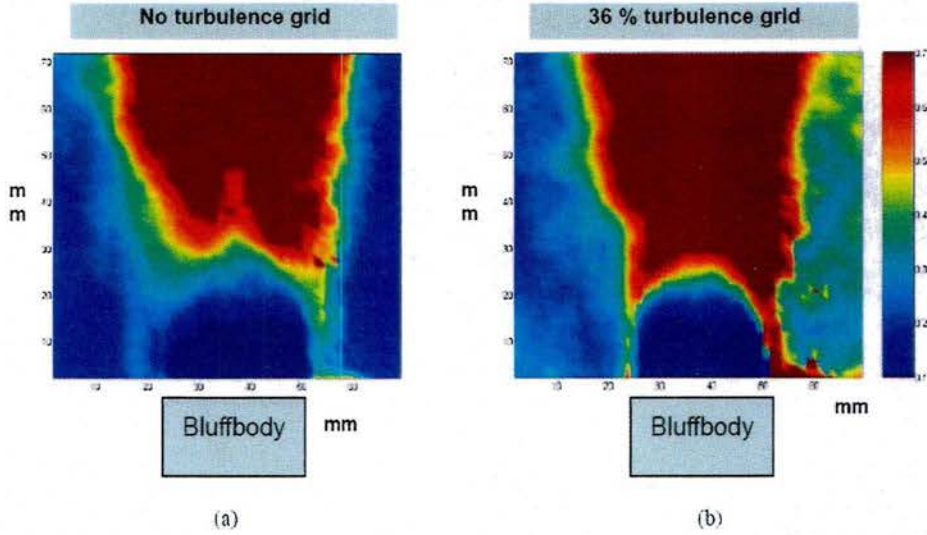


Figure 4: Turbulence intensities in the presence of bluff body, (a) no grid, (b) 36 % opening area grid. Imaging region is 1.5" higher than that of figure 3

quantified by investigating the liftoff height of an afterburning methane flame. As performed in Phase I, CH chemiluminescence of the flamebase is detected by a 100 s gate width intensified CCD camera (Princeton Instrument, PI-MAX) to determine instantaneous flamebase locations. The liftoff height is determined by an average over 200 ensembles of the instantaneous flamebase location.

Figure 6 shows a sample result of the flame liftoff height measurements under four different amounts of the  $\text{H}_2\text{O}_2/\text{H}_2\text{O}$  injections: no injection, 100 % water (20 sccm total), 30 %  $\text{H}_2\text{O}_2$  in 70 % water (20 sccm total), and 50 %  $\text{H}_2\text{O}_2$  in 50 % water (20 sccm total). We are limited to 50%  $\text{H}_2\text{O}_2$  due to safety considerations. Flow conditions are identical with those of Fig. 4 except for the injections. As shown, the flame stability decreases with increasing water concentration of the injection. In comparison with the no-injection case, for example, 100 % water injection decreases the flame stability by  $\sim 25$  %. However, the increasing  $\text{H}_2\text{O}_2$  portion in the injection reverses the propensity such that the flame stability of the 50 %  $\text{H}_2\text{O}_2$  addition is comparable with that of the no-injection case. It is noteworthy that, based on our preliminary PREMIX calculation (not shown here), more than 99.99 % of  $\text{H}_2\text{O}_2$  is dissociated to form  $\text{H}_2\text{O}$  at this temperature ( $\sim 1200$  K) within less than 1 ms while  $\sim 10^{-4}$  mole fraction OH radicals still linger. Therefore, increasing flame stability with increasing amounts of  $\text{H}_2\text{O}_2$  addition shown in this result provides plausible evidence on the central role of the OH radicals on the flame stability.

In summary, the results shown here provide a configuration for experimental studies to generate higher turbulence intensity and higher OH radical concentration in the post combustion

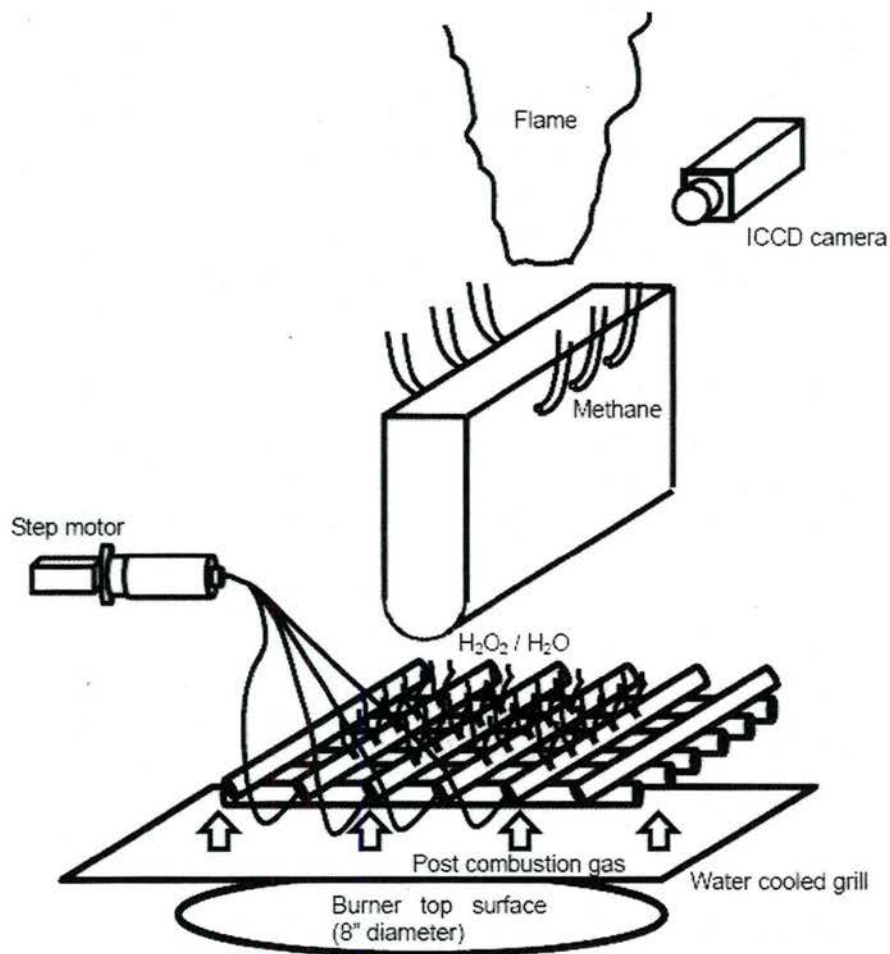


Figure 5: Turbulence intensities in the presence of bluff body, (a) no grid, (b) 36 % opening area grid. Imaging region is 1.5" higher than that of figure 3

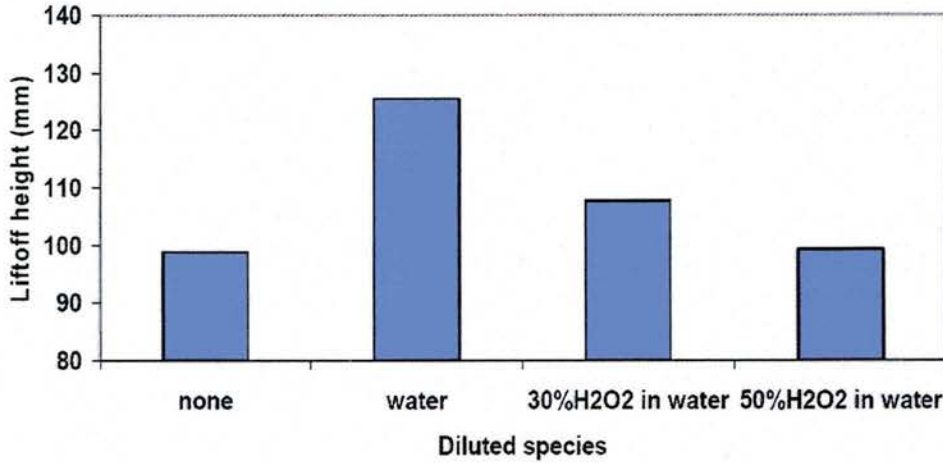


Figure 6: Flame liftoff heights under various amounts of  $\text{H}_2\text{O}_2/\text{H}_2\text{O}$  injections

stream. Future studies can allow a broader range of the turbulence intensity and the OH radical concentration, detailed measurements of the bluff-body shedding frequencies and spectra and simultaneous and instantaneous CH PLIF/PIV measurements using ethylene fuel for greater CH signals. Such results will provide a more comprehensive dataset which will allow a more careful determination of the effect of radical composition and the underlying flow field on bluff-body flame stability.

## 4.2 Modeling and Computation

### 4.2.1 Validation and Damköhler Number Similarity

Flame-holders provide two flame stability mechanisms. As the flame-holder modifies the flow around it, a wake is generated aft of the flame-holder base. This wake provides sufficient residence time and chemical heat release needed to ignite the fresh gas. In addition, the shear layer generated around the wake provides a turbulent mechanism to mix the fresh air with the combustion products from the recirculation zone [1, 2]. Finally, as the flame is stabilized past the flame-holder base, combustion products at the end of the recirculation zone are entrained into the wake to provide a self-ignition mechanism.

The inflow mixture to the augmentor usually has high speed and high temperature. The typical inflow temperature and velocity for augmentors range between 700–1000 K and 100–200 m/s respectively[3]. Under these conditions, the experimental assessment of such configurations is complex and expensive, and it becomes practically challenging to investigate the flow and combustion features. The current work investigates the possibility of utilizing similarity to test such configurations. Here, we will assess the Damköhler number similarity, which implies that in the high Reynolds number limit, the flow and the flame characteristics in a high-speed/fast

chemistry case should be similar to a low-speed/slow chemistry case, as long as the Damköhler number and all the momentum ratios is the same.

Here, three numerical simulations are performed using large-eddy simulations. The chemical source term is modeled using the flamelet progress variable (FPV) approach. The configuration is for a bluff-body stabilized flame in a vitiated cross-flow. Methane fuel is injected in the cross-stream direction from the bluff-body surface. The geometry of the bluff body is represented in the simulation by an immersed boundary technique on a structured grid. The combination of immersed boundary with structured codes gives the advantage of simulating complex geometries with lower computational cost and high accuracy because of the staggered variable arrangement. For constant Reynolds number, the inflow temperature and chemical composition are varied to change the mutual effect between mixing and chemical time scales, and hence the Damköhler number. The inflow chemical variation and the Damköhler number are found to affect both the flame stabilization and the lift-off characteristics. The stagnation point position in the wake of the bluff body and the lift-off height are monitored for both test cases to assess the Damköhler number similarity. This section is organized as follows: We will first present the numerical and modeling approaches used, the non-dimensional form of the governing equations, and the definition of the characteristic Damköhler number. Next, we will show the numerical setup and the geometry details. Finally, the results will be discussed.

**Numerical Formulation** - All simulations reported here were performed with the Stanford NGA code. The numerical scheme used here is based on a high order conservative finite differences [4, 5]. The governing equations are in the low Mach number formulation. The scheme is staggered in space and time [6]. The staggering allows for secondary conservation. Hence, no artificial damping is required and the scheme can allow for higher order accuracy [5]. However, in the following section we will focus only on the details of the combustion model and the Damköhler number similarity analysis.

By applying an implicit top hat filter denoted by an overline to the Navier Stokes equations and using the Favre decomposition, defined for a general variable  $\phi$  as  $\tilde{\phi} = \bar{\rho}\phi/\bar{\rho}$ , the continuity and the momentum equations can be written as:

$$\begin{aligned}\frac{\partial \bar{\rho}}{\partial t} + \frac{\partial \tilde{\rho} \tilde{u}_i}{\partial x_i} &= 0 \\ \frac{\partial \tilde{\rho} \tilde{u}_i}{\partial t} + \frac{\partial \tilde{\rho} \tilde{u}_i \tilde{u}_j}{\partial x_j} &= -\frac{\partial \bar{P}}{\partial x_i} + \frac{\partial \tilde{\sigma}_{ij}}{\partial x_j} - \frac{\partial \tau_{ij}}{\partial x_j}.\end{aligned}\tag{1}$$

Here,  $\tilde{u}_i$  is the filtered velocity,  $\bar{\rho}$  is the filtered density,  $\bar{P}$  is the filtered pressure, and the filtered shear stress is written as  $\tilde{\sigma}_{ij} = \mu \left( \frac{\partial \tilde{u}_i}{\partial x_j} + \frac{\partial \tilde{u}_j}{\partial x_i} \right) - \mu \frac{2}{3} \delta_{ij} \frac{\partial \tilde{u}_k}{\partial x_k}$ . The summation over repeated indices is implied and  $\mu$  is the dynamic viscosity. In the above equations, the influence of the statistical effect of the subgrid scales on the resolved scales is represented by the sub-filter stresses

$\tau_{ij} = \bar{\rho} (\widetilde{u_i u_j} - \widetilde{u_i} \widetilde{u_j})$ . The sub-filter stresses are modeled with an eddy viscosity assumption [7]:

$$\tau_{ij} = -2\mu_T \left( \widetilde{S}_{ij} - \frac{1}{3} \widetilde{S}_{mm} \delta_{ij} \right) + \frac{1}{3} q^2 \delta_{ij}, \quad (2)$$

where  $\widetilde{S}_{ij} = \frac{1}{2} \left( \frac{\partial \widetilde{u_i}}{\partial x_j} + \frac{\partial \widetilde{u_j}}{\partial x_i} \right)$  is the velocity strain rate, and  $q^2$  is the trace of the sub-filter stress tensor. The turbulent eddy viscosity  $\mu_T$  and  $q^2$  are modeled as:

$$\begin{aligned} \mu_T &= C_\mu \bar{\rho} \Delta^2 |\widetilde{S}| \\ q^2 &= 2C_k \bar{\rho} \Delta^2 |\widetilde{S}|^2. \end{aligned} \quad (3)$$

In these equations  $|\widetilde{S}| = \sqrt{2\widetilde{S}_{ij}\widetilde{S}_{ij}}$  and  $C_\mu$  and  $C_k$  are computed dynamically based on the approach introduced by Moin et al. [7]. The density  $\bar{\rho}$  is calculated from the state equation described in the next section. Under the low Mach number approximation [8], the acoustic modes are decoupled from the entropy and the vorticity modes. This approximation allows for a larger and more stable integration time step for Eqs. (1). A semi-implicit iterative technique is employed to integrate the above system of equations using the fractional step method. More details about the above numerical approach can be found elsewhere [6, 5] and hence are avoided here for brevity. The following section will describe the employed combustion model.

**Flamelet Progress Variable Approach** - The flamelet/progress variable (FPV) approach developed by Pierce and Moin [9] is based on the flamelet concept [10]. This approach assumes that the chemical time scales are fast enough such that the reactions occur in thin layers around the stoichiometric conditions [11]. The flamelet approach relates the species mass fractions and the energy to the mixture fraction through the flamelet equations [12]:

$$\rho \frac{\partial \Phi}{\partial t} - \rho \frac{\chi}{2} \frac{\partial^2 \Phi}{\partial Z^2} = \dot{\omega}, \quad (4)$$

where  $Z$  is the mixture fraction,  $\Phi = (T, y_i)^T$  is a vector that contains the species mass fractions  $y_i$  and the temperature  $T$ .  $\dot{\omega}$  is the source term and  $\chi$  is the scalar dissipation rate, which represents the inverse of the diffusion characteristic time scale or equivalently the fluid influence on the non-conserved scalars. In Eq. (4) the scalar dissipation rate is given by [13]

$$\chi = 2D|\nabla Z|^2. \quad (5)$$

In the FPV model, a new reactive scalar  $\lambda$  is introduced. As a result, the state vector is given as  $\Phi = \mathcal{F}_\Phi(Z, \lambda)$ . Accordingly, this formulation assumes that the reactive scalars are a function of  $Z$  and  $\lambda$ . Then

$$\tilde{\Phi} = \int_0^1 \int_0^\infty \Phi(Z, \lambda) \tilde{P}(Z, \lambda; x, t) d\lambda dZ. \quad (6)$$

The  $\lambda$ -parameter is represented by the progress variable  $C$  that can be a combination of certain species products, temperature, enthalpy or any scalar that can represent the reactive state

uniquely. The progress variable here is taken as the sum of the mass fractions of  $\text{CO}_2$ ,  $\text{CO}$ ,  $\text{H}_2\text{O}$ , and  $\text{H}_2$ . Then, also  $\tilde{C}$  can be obtained from Eq. 6, and  $\lambda$  can be eliminated from the problem. The passive scalar marginal PDF  $\tilde{P}(Z)$  is assumed to be a beta distribution [9], and the reactive scalar PDF as delta function. Since the PDF distribution is characterized by the scalar mean and the variance, the flamelet tabulation will take this form:

$$\tilde{\Phi} = \mathcal{F}_{\tilde{\Phi}}(\tilde{Z}, \widetilde{Z''^2}, \tilde{C}). \quad (7)$$

Therefore, three parameters have to be computed, namely the filtered mixture fraction  $\tilde{Z}$ , the sub-filter scalar variance  $\widetilde{Z''^2}$ , and the filtered progress variable  $\tilde{C}$ . Here the scalar variance  $\widetilde{Z''^2}$  is evaluated using an algebraic model [14]. The model assumes homogeneity and local equilibrium for the sub-grid scales and is given as

$$\widetilde{\rho Z''^2} = C_Z \Delta^2 \bar{\rho} |\nabla \tilde{Z}|^2, \quad (8)$$

where the mixture fraction coefficient  $C_Z$  is computed dynamically. The second parameter is the filtered mixture fraction  $\tilde{Z}$ , for which a transport equation is solved as

$$\frac{\partial \tilde{\rho} \tilde{Z}}{\partial t} + \nabla \cdot (\tilde{\rho} \tilde{u} \tilde{Z}) = \nabla \cdot (\tilde{\rho} (D_Z + D_T) \nabla \tilde{Z}). \quad (9)$$

The mixture fraction diffusivity  $D_Z$  is obtained from Eq. (6), and  $D_T$  is the turbulent eddy diffusivity given by [14]

$$D_T = C_T \Delta^2 |\tilde{S}|, \quad (10)$$

where  $C_T$  is computed in a dynamic procedure [7]. Finally, the filtered progress variable is obtained by solving the transport equation of  $\tilde{C}$  as:

$$\frac{\partial \tilde{\rho} \tilde{C}}{\partial t} + \nabla \cdot (\tilde{\rho} \tilde{u} \tilde{C}) = \nabla \cdot (\tilde{\rho} (D_C + D_T) \nabla \tilde{C}) + W_C, \quad (11)$$

where  $D_C$  is the progress variable diffusivity, and  $W_C = \widetilde{\rho(\dot{m}_C/\rho)}$  is the Favre averaged net mass production rate of  $C$ ,  $\dot{m}_C$  is the unfiltered net production rate in ( $\text{kg}/\text{m}^3/\text{sec}$ ). In the above formulation, given the mean and the variance, the subgrid fluctuations effect on the filtered state vector  $\tilde{\Phi}$  is represented by the integration over the joint PDF of  $Z$  and  $C$  expressed in Eq. (6) [15]. Next we will reformulate the governing equations in the non-dimensional form to show the dependence on the Damköhler number and the similarity conditions.

**Non-Dimensional Governing Equations** - To derive the non-dimensional governing equations, the following relations are defined, where the subscript  $(\infty)$  refers to the reference values

at the vitiated inflow conditions and the superscript (\*) refers to the non-dimensional values:

$$\begin{aligned}
\tilde{u}_i^* &= \frac{\tilde{u}_i}{U_\infty}, & x_i^* &= \frac{x_i}{D_b}, & \bar{\mu}^* &= \frac{\bar{\mu}}{\mu_\infty} \\
\mu_T^* &= \frac{\mu}{\rho_\infty U_\infty D_b}, & t^* &= \frac{t U_\infty}{D_b}, & \tilde{C}^* &= \frac{\tilde{C}}{C_\infty} \\
\bar{\rho}^* &= \frac{\bar{\rho}}{\rho_\infty}, & \bar{P}^* &= \frac{\bar{P}}{\rho_\infty U_\infty^2}, & D_C^* &= \frac{D_C}{D_{C,\infty}}, \\
D_Z^* &= \frac{D_Z}{D_{Z,\infty}}, & D_T^* &= \frac{D_T}{U_\infty D_b}, & \chi^* &= \frac{\chi}{\chi_q}.
\end{aligned} \tag{12}$$

Here the reference length scale is chosen as the bluff-body diameter  $D_b$ . In the following analysis, the inflow progress variable diffusivity  $D_{C,\infty}$  and the inflow mixture fraction diffusivity  $D_{Z,\infty}$  are fixed to a single value  $D_\infty$  that corresponds to the maximum inflow diffusivity. Another important parameter  $r = \sqrt{\frac{2\rho_j U_j^2}{\rho_\infty U_\infty^2}}$  is the momentum ratio between the fuel jet (subscript  $j$ ) and the vitiated oxidizer stream (subscript  $\infty$ ). The scalar dissipation rate  $\chi$  is non-dimensionalized by its value at the quenching conditions  $\chi_q$ . Note that the mixture fraction as a normalized quantity needs no further normalization.

By substitution of Eqs. (12) in Eqs. (1) (and dropping the \*), we get the following non-dimensional form:

$$\begin{aligned}
\frac{\partial \bar{\rho}}{\partial t} + \frac{\partial \bar{\rho} \tilde{u}_i}{\partial x_i} &= 0, \\
\frac{\partial \bar{\rho} \tilde{u}_i}{\partial t} + \frac{\partial \bar{\rho} \tilde{u}_j \tilde{u}_i}{\partial x_j} &= -\frac{\partial \bar{P}}{\partial x_i} + \frac{1}{\text{Re}_\infty} \left( \frac{\partial \tilde{\sigma}_{ij}}{\partial x_j} \right) - \frac{\partial \tau_{ij}}{\partial x_j},
\end{aligned} \tag{13}$$

where the vitiated inflow Reynolds number is given by  $\text{Re}_\infty = \frac{\rho_\infty U_\infty D_b}{\mu_\infty}$ . In Eq. (13), the subgrid models presented by Eq. (3) are used to non-dimensionalize the sub-filter stresses  $\tau_{ij}$ . Following the same procedure with Eqs. (9) and (11), we get the filtered progress variable and the filtered mixture fraction equations in the non-dimensional form as

$$\frac{\partial \bar{\rho} \tilde{Z}}{\partial t} + \frac{\partial}{\partial x_i} (\bar{\rho} \tilde{u}_i \tilde{Z}) = \frac{1}{\text{Re}_\infty \text{Sc}_\infty} \left( \frac{\partial}{\partial x_i} \left( \bar{\rho} D_Z \frac{\partial \tilde{Z}}{\partial x_i} \right) \right) + \frac{\partial}{\partial x_i} \left( \bar{\rho} D_T \frac{\partial \tilde{Z}}{\partial x_i} \right), \tag{14}$$

$$\frac{\partial \bar{\rho} \tilde{C}}{\partial t} + \frac{\partial}{\partial x_i} (\bar{\rho} \tilde{u}_i \tilde{C}) = \frac{1}{\text{Re}_\infty \text{Sc}_\infty} \left( \frac{\partial}{\partial x_i} \left( \bar{\rho} D_C \frac{\partial \tilde{C}}{\partial x_i} \right) \right) + \frac{\partial}{\partial x_i} \left( \bar{\rho} D_T \frac{\partial \tilde{C}}{\partial x_i} \right) + \text{Da}_c W_C^*, \tag{15}$$

where  $\text{Sc}_\infty = \frac{\mu_\infty}{\rho_\infty D_\infty}$  is the vitiated inflow Schmidt number for the scalar progress variable and the mixture fraction and the non-dimensional source term and the Damköhler number  $\text{Da}_c$  will be introduced below. Further treatment for the progress variable source term will be discussed

in the next subsection. Finally, the state relationship for the thermodynamic and chemical variables is computed from the non-dimensional equation of state:

$$\Phi^* = \mathcal{F}_{\tilde{\Phi}}(\tilde{Z}, \tilde{C}^*) . \quad (16)$$

For the same non-dimensional quantities (i.e.  $Re_\infty$ ,  $Sc_\infty$ , and  $Da_c$ ), Eqs. (13)-(16) will have the same solution for similar boundary conditions. The inflow boundary conditions for the cross flow and the jet are uniform with bulk velocity  $U_\infty$  and  $U_j$  respectively. Therefore, the inflow boundary conditions for the vitiated cross flow in the non-dimensional form will be:

$$\begin{aligned} u_{1,\infty}^* &= 1.0 \\ u_{2,\infty}^* &= 0.0 \\ u_{3,\infty}^* &= 0.0 \\ C_\infty^* &= 1.0 \\ Z &= 0.0 . \end{aligned} \quad (17)$$

Similarly, the non-dimensional jet inflow conditions will be:

$$\begin{aligned} u_{1,j}^* &= 0.0 \\ u_{2,j}^* &= 0.0 \\ u_{3,j}^* &= \frac{r}{\sqrt{2\rho_j^*}} \\ C_j^* &= 0.0 \\ Z &= 1.0 . \end{aligned} \quad (18)$$

where  $r = \sqrt{\frac{2\rho_j U_j^2}{\rho_\infty U_\infty^2}}$  is the momentum ratio, and  $\rho_j^* = \frac{\rho_j}{\rho_\infty}$ . The convective condition is used for the outflow boundary. This condition can be written for a general variable  $\psi$  as:

$$\frac{\partial \psi}{\partial t} + a \frac{\partial \psi}{\partial x_n} = 0 , \quad (19)$$

where  $a$  is the convection speed at the outflow cross-section, and  $x_n$  is the coordinate in the direction of the outward normal at the boundary. In the non-dimensional form this equation can be written as:

$$\begin{aligned} \frac{\partial \tilde{u}_i^*}{\partial t} + a^* \frac{\partial \tilde{u}_i^*}{\partial x_n} &= 0 \\ \frac{\partial \tilde{C}^*}{\partial t} + a^* \frac{\partial \tilde{C}^*}{\partial x_n} &= 0 \\ \frac{\partial \tilde{Z}}{\partial t} + a^* \frac{\partial \tilde{Z}}{\partial x_n} &= 0 . \end{aligned} \quad (20)$$

The above equations show that given two different test cases, with the same momentum ratio ( $r$ ) and the same non-dimensional reference quantities (i.e.  $Re_\infty$ ,  $Sc_\infty$ , and  $Da_c$ ), the set of

Eqs. (13)-(15) will have similar boundary conditions and similar solution. However, in the next subsection the source term in Eq. (15) will be discussed in more details.

**Damköhler Number Similarity** - The characteristic Damköhler number is defined as the ratio between the characteristic flow or mixing time scale to the characteristic chemical time scale

$$Da_c = \frac{\tau_{\text{flow}}}{\tau_{\text{chem}}} \quad (21)$$

where the flow time scale is defined as  $\tau_{\text{flow}} = \frac{D_b}{U_\infty}$ , based on the bluff-body width  $D_b = 25.4$  mm and the cross flow velocity  $U_\infty$ . The chemical time scale can be defined by many different methods. For single step chemistry, it is typically defined as the chemical source term divided by a reactant concentration. In a previous work, Pitsch and Fedotov [16] derived an expression for the non-dimensional source term for a single step chemistry. They showed that the source term and equivalently the chemical time scale are a function of unique non-dimensional quantities that depend on the frequency factor of the one-step mechanism and the chemical and thermal boundary conditions. However, detailed chemical mechanisms describe many combustion phenomena, such as auto-ignition, premixed flame propagation, and non-premixed combustion. Because of the different interactions of these processes with molecular transport, different chemical reactions might be important in these processes, and there is no unique definition of the relevant chemical time scale. Each chemical reaction has its own time-scale and Damköhler number. If a similar solution is to be achieved, for instance, at a higher flow velocity, which implies a smaller flow time scale, also the chemical time scales need to be reduced to achieve the same Damköhler numbers. Typical ways to change the chemical time scales are changes in the temperature, the equivalence ratio, or dilution. It is obvious that not all chemical time scales can be changed in the same way. Therefore, the choice of the adjusted chemical time scale should be related to the physics of the dominating combustion phenomenon. For example, in premixed flames, the flame response based on the flame thickness and flame propagation speed is more relevant. For non-premixed flames, the chemical time scale should represent the mutual interaction between chemistry and mixing. The following analysis shows that for the problem in consideration the vitiated inflow temperature, for a given inflow speed, has a strong effect on the available range of chemical time scales and on the ignition and quenching characteristics. As shown in Fig. 7, as the vitiated inflow temperature increases, the production rate of certain species is accelerated, and the mixture is ignited at a faster chemical time scale. This increases the strain rate and the mixture fraction gradient, and allows for a higher quenching scalar dissipation rate as well. As the inflow temperature increases more, around  $T_\infty = 1700$  K the mixture is self-ignited and the lower unstable branch disappears.

Figure 8 shows the non-dimensional source term versus the non-dimensional dissipation rate for different vitiated inflow temperatures. The source term in Eq. (15) will be non-dimensionalized

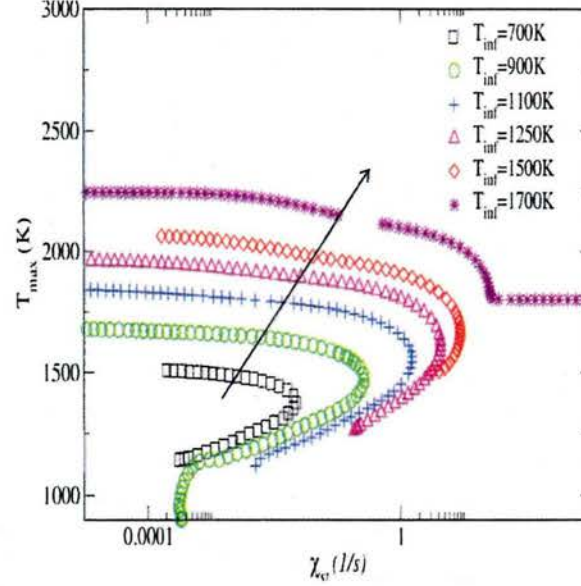


Figure 7: The effect of the vitiated hot flow temperature ( $T_{inf}$ ) on quenching and ignition characteristics of the flamelets at the stoichiometric conditions

with the maximum progress variable production rate  $W_{C,max}$  as

$$W_C^* = \frac{W_C}{W_{C,max}}. \quad (22)$$

The corresponding characteristic chemical time scale is then

$$\tau_{chem} = \frac{\rho_\infty C_\infty}{W_{C,max}}, \quad (23)$$

and the Damköhler number becomes

$$Da_c = \frac{D_b W_{C,max}}{U_\infty \rho_\infty C_\infty}. \quad (24)$$

It is obvious that the minimum chemical time scale appears approximately at stoichiometric mixture fraction. To illustrate this observation, Fig. 9 shows a scatter plot of the inverse of the local chemical time scale with the mixture fraction. The minimum chemical time scale that corresponds to the highest production rate is located at the stoichiometric condition. As will be shown next, the value of the production rate at quenching is slightly lower than the maximum value.

Further insight can be achieved by plotting the three dimensional S-shaped curve in Fig. 10, which shows the maximum temperature and the chemical time scale as function of the dissipation rate. The curve shows that the upper and lower branch have different time scales, which is even more clear in Fig. 10b. For the burning branch the chemical time scale is smaller. As also shown

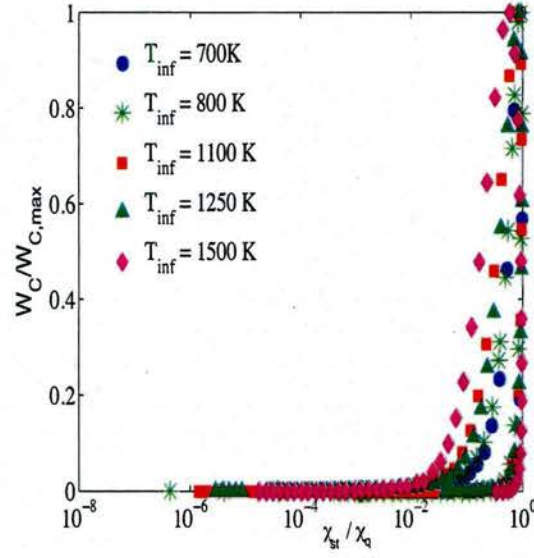


Figure 8: The variation of the non-dimensional progress variable production rate with the non-dimensional scalar dissipation rate

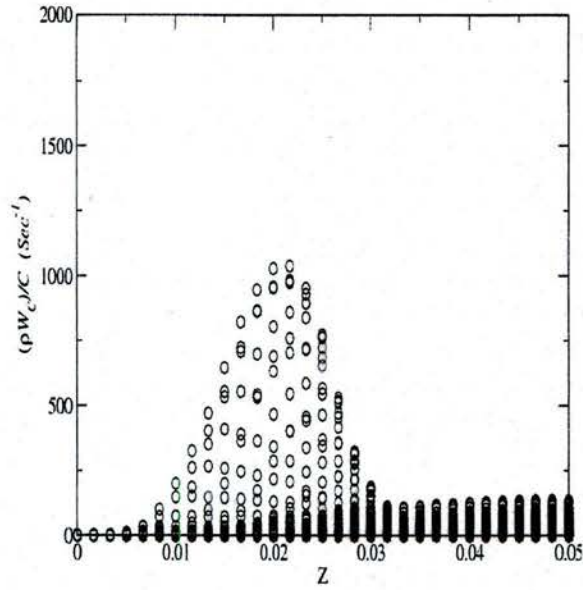


Figure 9: Scatter plot for the inverse of the local chemical time scale with the mixture fraction

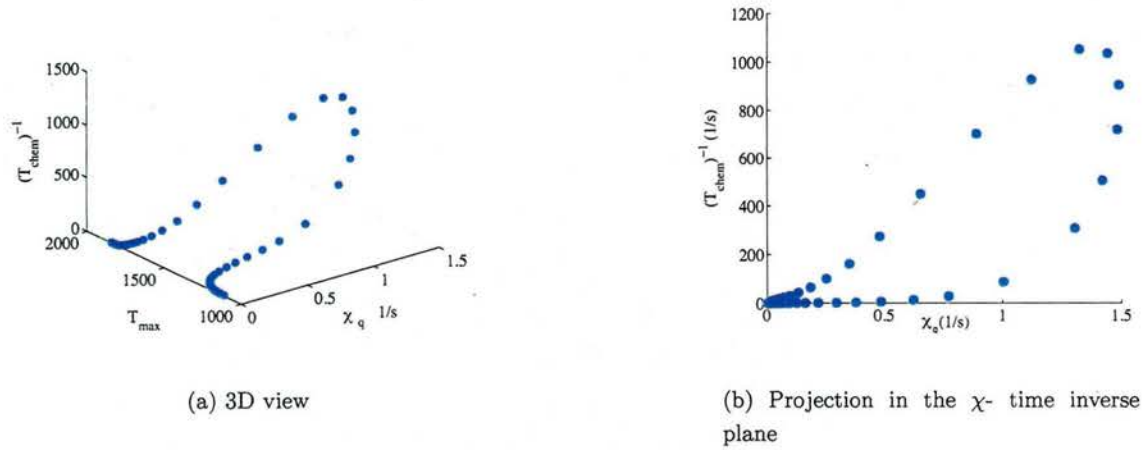


Figure 10: Three dimensional S-shaped curve

in Fig. 10b, the value of the chemical time scale at the quenching point is slightly higher than the minimum value.

It should be noted again that here the characteristic chemical time scale is defined as the lowest possible time scale at stoichiometric conditions. This time scale corresponds to the maximum Damköhler number for a given flow condition.

**Numerical Setup** - The bluff-body geometry and the grid after refinement are shown in Fig. 11. Methane jets at 300 K are injected from two circular ports 0.5 inch upstream the base of the bluff body. A flow of vitiated hot mixture is injected in the stream-wise direction. The jet and the vitiated mixture mass flow rates are varied to change the effective flow time and hence the Damköhler number. The bluff body is 4.5 inch long with a 1 inch width rectangular body and a 1/2 inch radius rounded nose.

Since the current work is devoted to the validation and assessment of the similarity solution, three different test cases are chosen here. The flow conditions for the three test cases are summarized in Table 1.

The conditions of the first test case match the setup of the Stanford vitiated flow experiment, while in the other two cases the flow and the chemical conditions are varied such that the Damköhler number is kept the same. The first test case represents low-speed/slow chemistry, while the second and the third case represent high-speed/fast chemistry. The inflow composition is computed as the equilibrium composition of methane/air at the inflow equivalence ratio and temperature. These values are then used as an input to the flamelet equations boundary conditions.

**Results** - The instantaneous recirculation zones (RZ) and flame structures for all three cases are shown in Fig. 12. The three flames show similar flame and RZ structure. The recirculation zone is found to extend over the bluff-body base and is surrounded by the flame surface. The

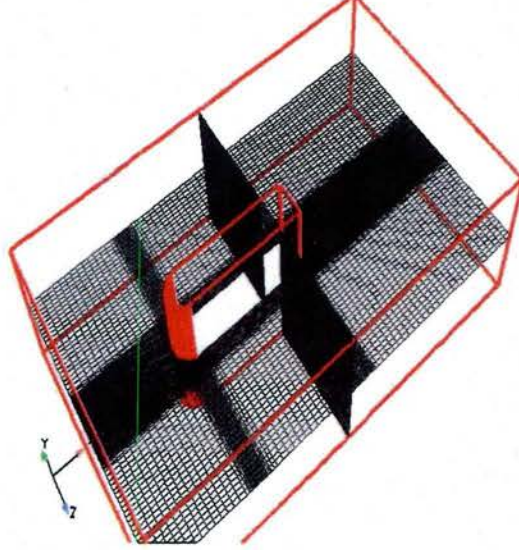


Figure 11: Computational mesh for LES of the flame holder geometry

Case#	$U_\infty$	$U_j$	$r$	$T_\infty(K)$	$\mu_\infty$	$D_\infty$	$\Phi_\infty$	$\tau_{flow}$	$\tau_{chem}$	$Da_c$	$Re_\infty$	$Sc_\infty$
Case 1	3.6	2.23	1.3	1100	1.6E-5	0.1E-3	0.67	0.0071	0.0011	6.429	5715	0.16
Case 2	7.8	4.43	1.3	1300	3.45E-5	0.22E-3	0.67	0.00327	0.00051	6.429	5715	0.16
Case 3	22.7	9.75	1.3	1700	1.E-4	4.23E-3	0.67	0.00118	1.74E-4	6.429	5715	0.16

Table 1: Flow test conditions, where  $\Phi_\infty$  and  $T_\infty$  are the equivalence ratio and the temperature of the vitiated hot stream respectively,  $\mu_\infty$  is the inflow kinematic viscosity in ( $m^2/s$ ),  $D_\infty$  is the inflow molecular mass diffusivity ( $m^2/s$ ),  $U_\infty$  is the vitiated air bulk velocity in ( $m/s$ ),  $U_j$  is the fuel jet velocity in ( $m/s$ ),  $\tau_{flow}$  is the characteristic flow time in seconds,  $\tau_{chem}$  is the characteristic chemical time in seconds,  $Da_c$  is the characteristic Damköhler number, and  $Re_\infty$ , and  $Sc_\infty$  are the vitiated hot flow Reynolds number and Schmidt number respectively.

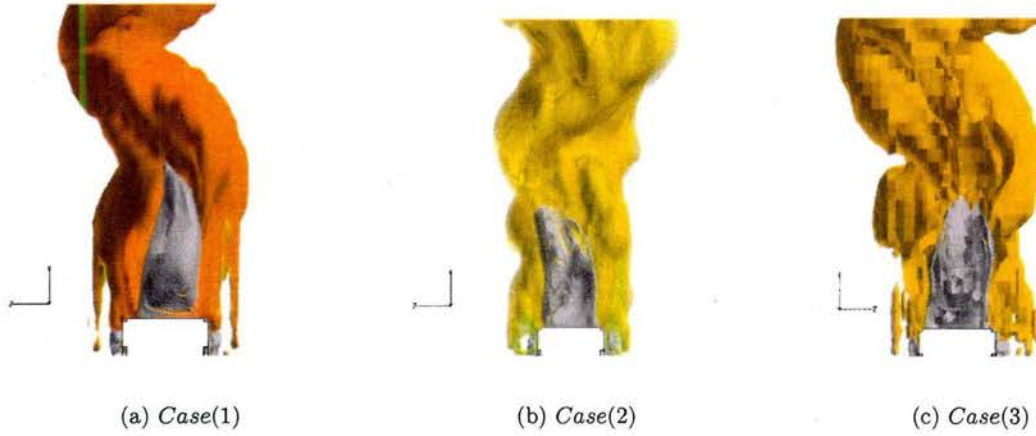


Figure 12: The iso-surface of negative axial velocities (grey) combined with the temperature iso-surface colored by the progress variable

effect of the outer shear layer is shown to wrinkle the flame surface, causing shedding of mixed burned/unburned gases towards the outflow. More discussion will be provided below.

Figure 13 shows the mean non-dimensional axial velocity distributions at different heights above the bluff-body base. The RZ extends to a distance of around 50 mm above the base. The wake extends about 20 mm in both directions of the centerline. Experimental data are available at three locations and are compared with the simulation results. Good agreement is noticed between the LES and the experimental data. However, the LES data show a symmetrical solution, while the experimental data do not. This asymmetry in the experimental results is due to the fact that the inflow field is not perfectly uniform. Most importantly here, the non-dimensional curves collapse onto each other, which confirms the flow similarity of the three flames.

A comparison of the normalized mean temperature is shown in Fig. 14. The three test cases exhibit the same flame structure. However, at the first location, the case (3) flame shows a small deviation at the edge of the shear layer. At this location, the effect of the unsteadiness due to the RZ oscillation contributes to this deflection as will be discussed later. The above results show that the mean flame and RZ structure exhibit a similarity solution under the given conditions for the three studied flames.

As the studied flames show similar RZ structure, they also show similar flame stability features. The flame stabilization point is defined as the first point where the flame and the flow speed match. Since this flame is wake stabilized, the wake structure controls the flame stability characteristics. Furthermore, as long as the chemical time scale is fast enough compared with the flow time scales, the flame will stabilize and will not blowoff. The faster the chemical time scale, the higher the flow speed needed to stabilize the flame at the same height. This finding ascertains the existence of Damköhler number similarity between the three flames. To further assess the validity of the current approach, the flame height above the base is measured and

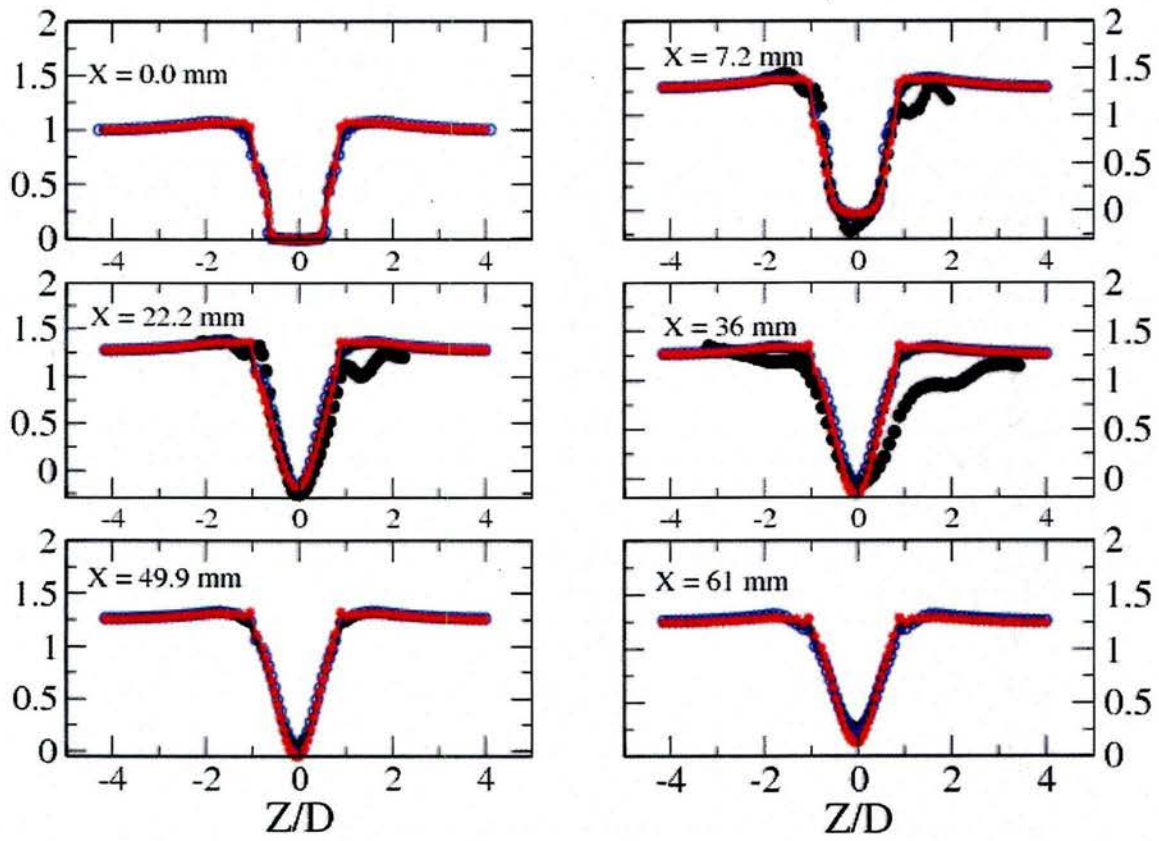


Figure 13: Mean non-dimensional axial velocity ( $\langle \frac{\bar{v}}{U_\infty} \rangle$ ) at different heights  $X$  above the bluff-body base; • experimental PIV data, (—) case (1), (—) case (2), (—) case (3)

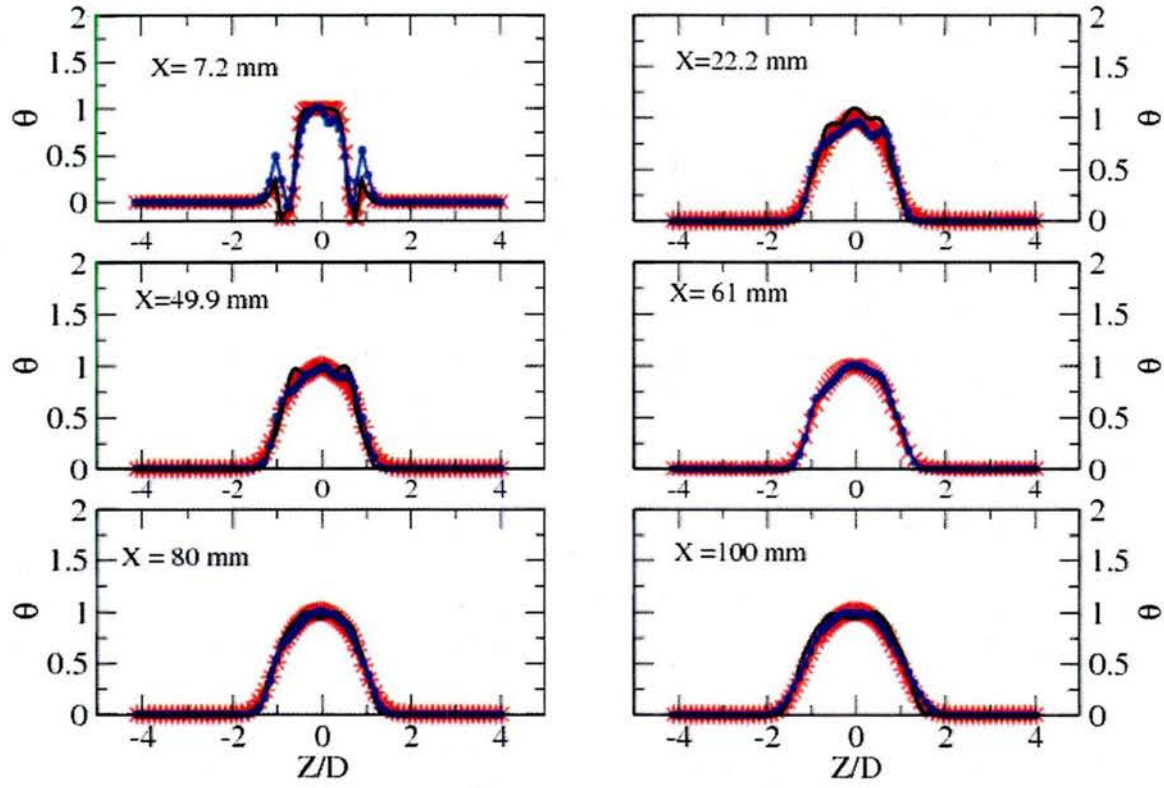


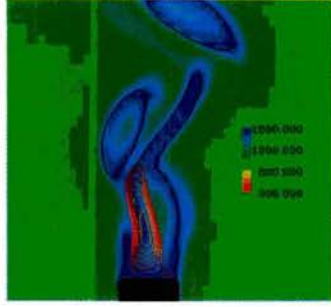
Figure 14: Mean normalized temperature ( $\Theta = \frac{\bar{T} - T_\infty}{T_{st} - T_\infty}$ ) at different heights above the bluff-body base, (—) case (1), (★) case (2), (○) case (3).  $T_{st}$  is the maximum burning temperature at stoichiometric conditions

compared with experimental data. By analogy with the experiment, the flame height is defined as the first point above the base (at the median plane), where the stoichiometric conditions are found. The flame height is computed as the average over the entire instantaneous snapshots. The averaged computed values are around 10.5 mm, 11.6 mm, and 13.2 mm for the three test cases, respectively, which are comparable to the experimentally reported value of 12 mm.

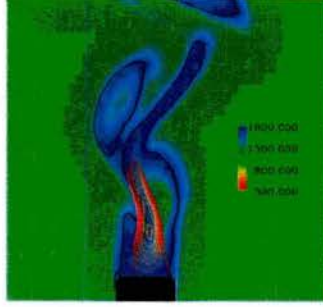
Next the flame/wake dynamics are discussed to illustrate the effect on the Damköhler number similarity. Only the first two flames will be compared here for brevity. Similar conclusions can be derived for the third case. In the low speed/slow chemistry flame (case 1), the RZ tip is found to be oscillating with a 10 Hz frequency in the spanwise direction. Figure 15 shows eight instantaneous snapshots at the plane  $Y = 10 \text{ mm}$  for case (1) over a complete cycle. The temperature field is combined with the contour of zero axial velocity to show the extension of the recirculation zone. The flame boundaries are shown by plotting the contour of the stoichiometric mixture fraction ( $Z = 0.021$ ). As the RZ tip oscillates, the strain rate changes across the flame surface. The RZ oscillation combined with the external shear layer (at the flame edge) result in burned gasses shedding, where alternative regions of hot and fresh gases are separated at the end of the RZ and convect downstream. The unburned regions can grow in size as they progress downstream or they can remix with hot gases and burn. The RZs in these cases provide sufficient residence time to mix the fresh gases and allow for burning. Starting from Fig. 15a, the RZ engulfs hot gases from its tip and recirculates hot products from the left side to burn the fresh gases on the right (see Fig. 15a-15f). This in turn allows the hot gases from the left side to convect downstream and mix with the fresh gas coming with the shear layer. At the edge of the RZ, quenching spots show up again due to the high strain rate. These quenching spots from the left side of the RZ shed downstream and mix with the downstream hot gases as shown in Fig. 15d-15h. At the end of the cycle, the RZ mixes burned gases from the right with the fresh incoming gases from the left (Fig. 15f-15i). This process is repeated every cycle on both sides to act as a natural self-ignition mechanism.

The same analysis is performed for test case (2) in Fig. 16. The flame shows wake and flame structure similar to the first flame. The RZ extends around 50 mm above the bluff-body base. The oscillation frequency is higher (about 50 Hz) as the residence time is smaller in this case. However, the RZ shows another mode of instability, where the flame is detached from the base, then reattaches at a 15 Hz frequency (Fig. 16g). This detachment is a result of the higher axial pressure gradient which overcomes the adverse pressure gradients at every cycle. The flame shows less coherent structures than test case (1). As shown in Fig. 15 and Fig. 16, as long as the two flames show similar stability dynamics, they will exhibit Damköhler number similarity for the mean flame and wake structures.

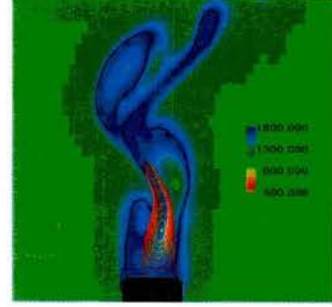
**Conclusion** - The validity of Damköhler number similarity for static stability in augmentor flows is shown. The high-speed/fast chemistry flame shows similar recirculation zone features and flame structure as the low-speed/slow chemistry flames. A characteristic Damköhler number is defined based on the maximum progress variable production rate. The flame stability and



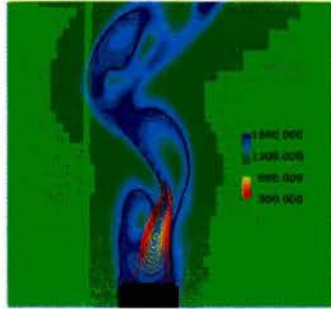
(a)  $T_1$



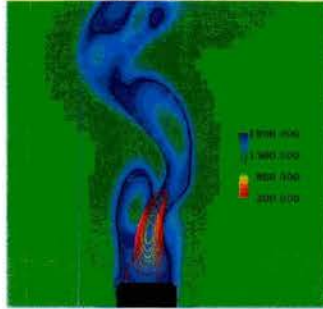
(b)  $T_2$



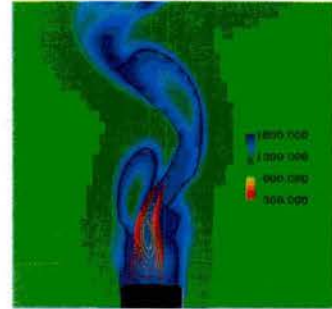
(c)  $T_3$



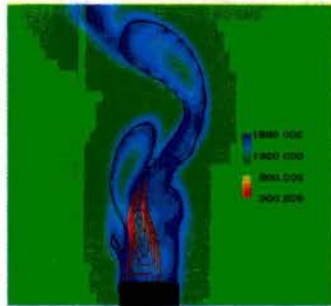
(d)  $T_4$



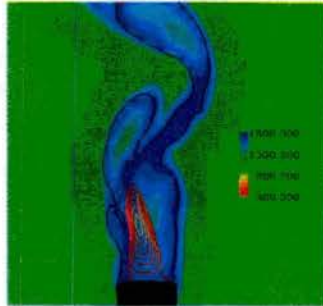
(e)  $T_5$



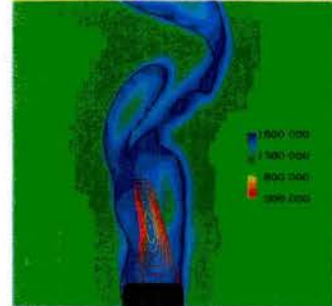
(f)  $T_6$



(g)  $T_7$

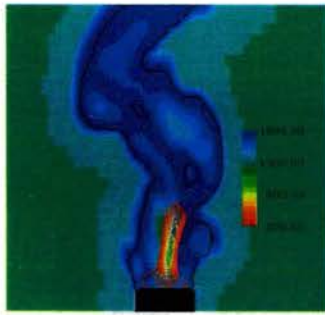


(h)  $T_8$

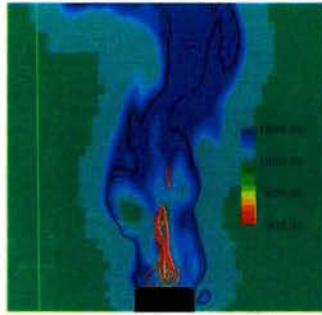


(i)  $T_9$

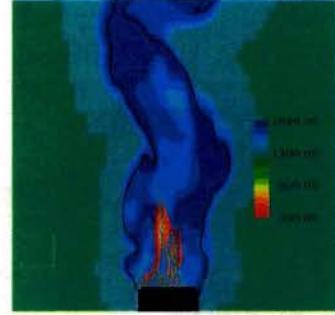
Figure 15: Instantaneous temperature distributions for case (1) at  $Y = 10 \text{ mm}$  combined with the contour of zero axial velocity (blue line) and the contour of stoichiometric mixture fraction (black line) over a complete cycle



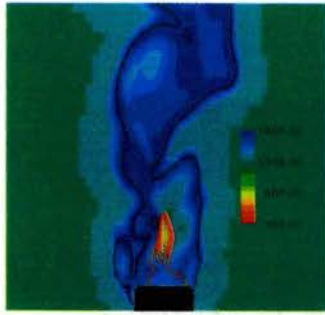
(a)  $T_1$



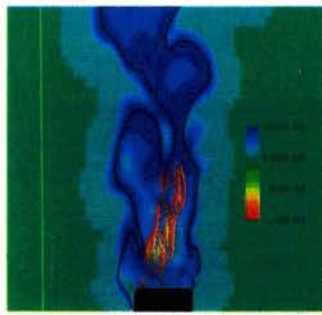
(b)  $T_2$



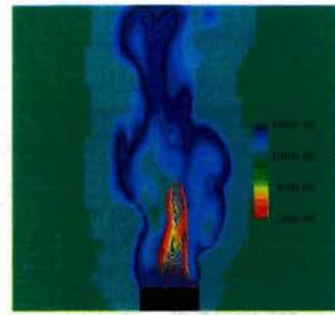
(c)  $T_3$



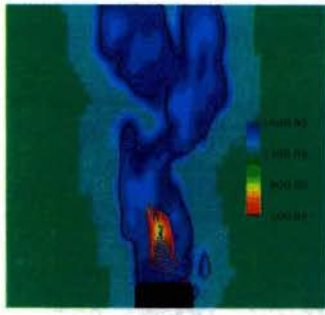
(d)  $T_4$



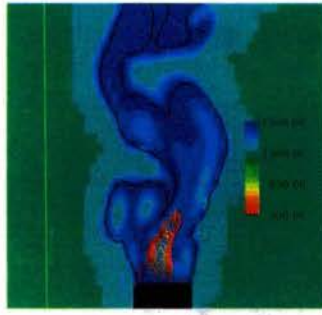
(e)  $T_5$



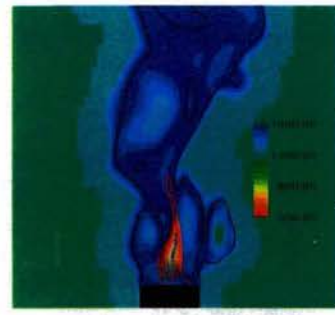
(f)  $T_6$



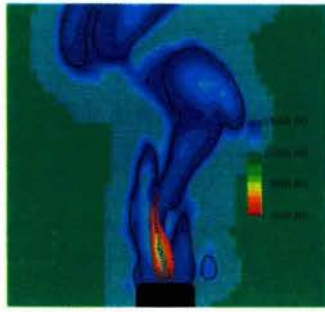
(g)  $T_7$



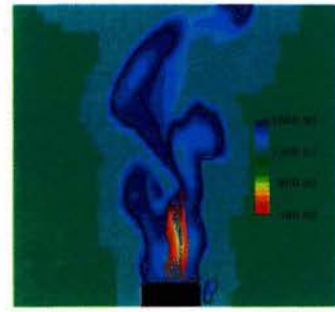
(h)  $T_8$



(i)  $T_9$



(j)  $T_{10}$



(k)  $T_{11}$

Figure 16: Instantaneous temperature distributions for case (2) at  $Y = 10 \text{ mm}$  combined with the contour of zero axial velocity (blue line) and the contour of stoichiometric mixture fraction

main characteristics are found to be controlled mainly by the wake dynamics.

#### 4.2.2 Large-Eddy Simulations of AFRL Flame Holder Experiment

The present section describes several simulations that have been performed for the planned experiments at AFRL. The aim here is to assess flow and flame stability and to compare with experimental data. Several simulations have been performed to compare different flow and combustion effects and turbulence models. We have performed reactive and non-reactive simulations using a structured LES flow solver, where the test rig geometry and the geometry of the flame holder are considered using the immersed boundary method. It is shown that, as expected from the flow regime, both the non-reactive and the reactive simulations lead to a stable flow. We have further performed non-reactive simulations on unstructured meshes using the CharLES flow solver. Further, we have performed unsteady 2D RANS simulations to assess the potential of low fidelity simulations. It is found that the 2D URANS simulations incorrectly show vortex shedding even for the non-reactive flow. In the following, we will first describe the flow conditions that have been chosen for all simulations followed by the simulation results.

**Flow Conditions** - Flow conditions have been chosen to fall in a range that is stable both for combustion and flow. A stoichiometric propane/air mixture is supplied at the inlet. Inflow velocity, kinematic viscosity, and inlet temperature are specified as

$$U_{\text{inflow,bulk}} = 45.72 \text{ m/s} \quad (25)$$

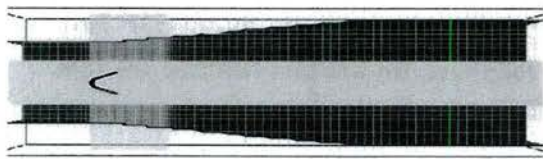
$$\nu = 2.0713 \cdot 10^{-5} \text{ m}^2/\text{s} \quad (26)$$

$$T_{\text{inflow}} = 433.0 \text{ K} . \quad (27)$$

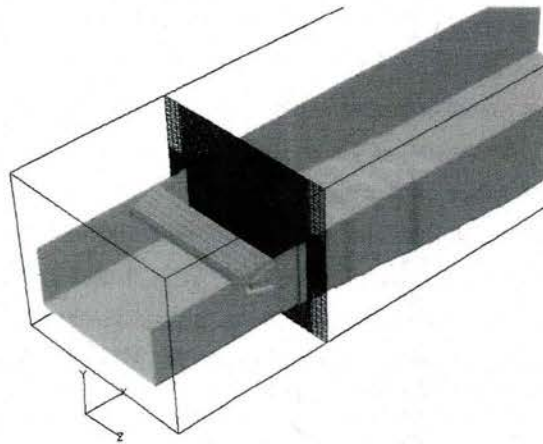
These parameters lead to a DeZubay parameter of approximately 30.

**Structured Flow Solver Cold Flow Results** - The structured mesh uses  $133 \times 126 \times 108$  cells in the  $x$ ,  $y$ , and  $z$  directions, and is shown in Fig. 17. Figure 18 shows the isosurface of the zero axial velocity. A two-dimensional snapshot of the axial velocity combined with the recirculation zone iso-surface is shown in Fig. 19. The corresponding time averaged axial velocity and RZ iso-surface are shown in Fig. 20, and the mean profile of the axial velocity is given in Fig. 21.

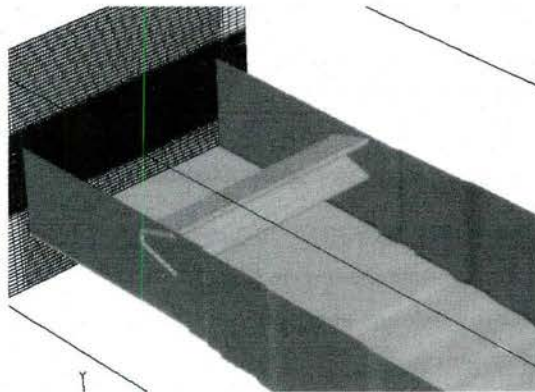
**Structured Flow Solver Reactive Flow Results** - For this case, the Inflow conditions are the same as for the non-reactive case. A combined level set/flamelet progress variable model by Knudsen and Pitsch [17] developed at Stanford under AFOSR funding is used for these simulations. The laminar flame speed for the computed conditions is 85.933 m/s, and the laminar flame thickness is 0.398761 mm. Figure 22 shows an instantaneous snapshot of the temperature distribution. Figures 23 and 24 show instantaneous snapshots of the carbon-monoxide and the progress variable distribution, respectively. It is obvious from these figures that because of the long residence time within the V-gutter cavity, the mixture is fully reacted



(a) Y-Z plane



(b) Z-X plane



(c) 3D cut view from the outflow direction

Figure 17: AFRL V-gutter geometry and structured mesh

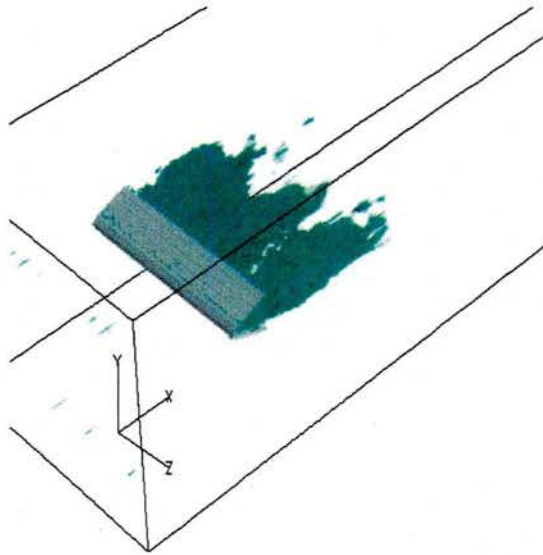


Figure 18: Instantaneous snapshot of the recirculation zone ( $U = 0$  m/s iso-surface)

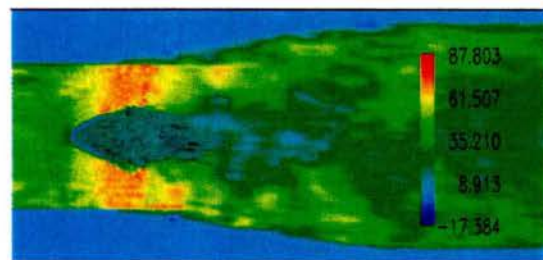


Figure 19: Instantaneous snapshot of the axial velocity component at the  $Z = 0.0$  plane

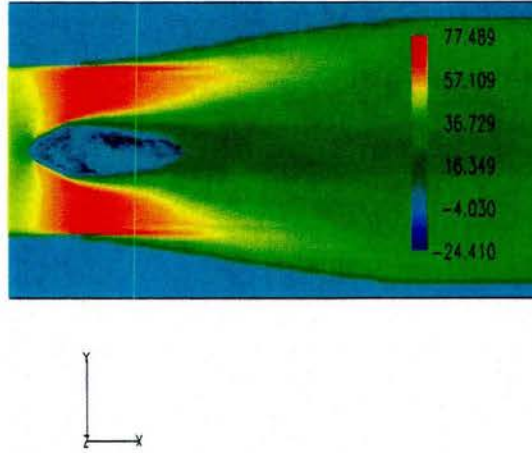


Figure 20: Time averaged axial velocity component at the  $Z = 0.0$  plane combined with the RZ iso-surface

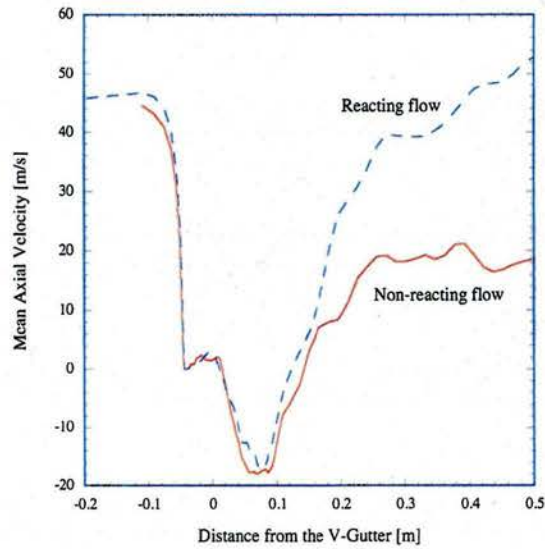


Figure 21: Time averaged axial velocity profile at  $Z = 0.0$  and  $Y = 0.0$

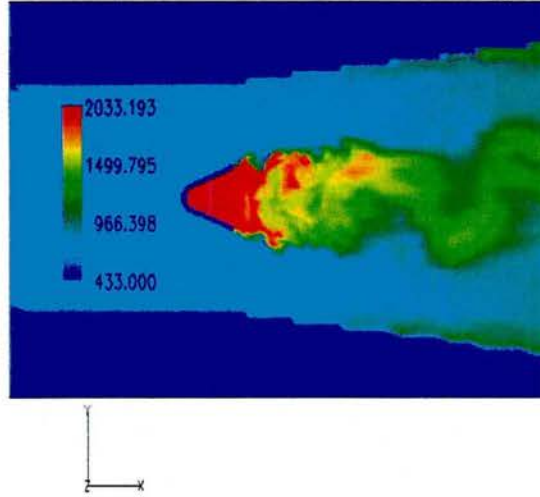


Figure 22: Instantaneous snapshot of temperature distribution at plane  $Z = 0$

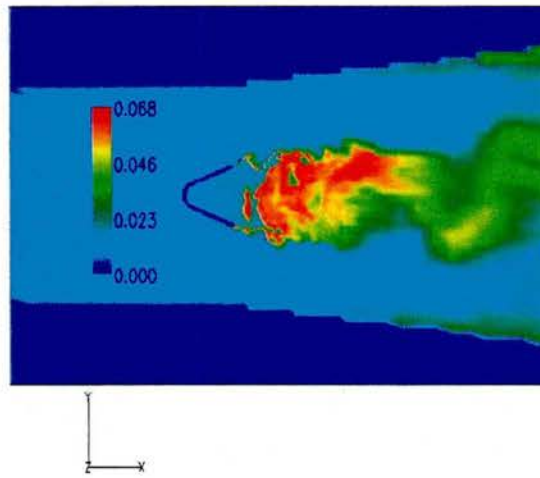


Figure 23: Mass fraction of carbon monoxide at plane  $Z = 0$ .

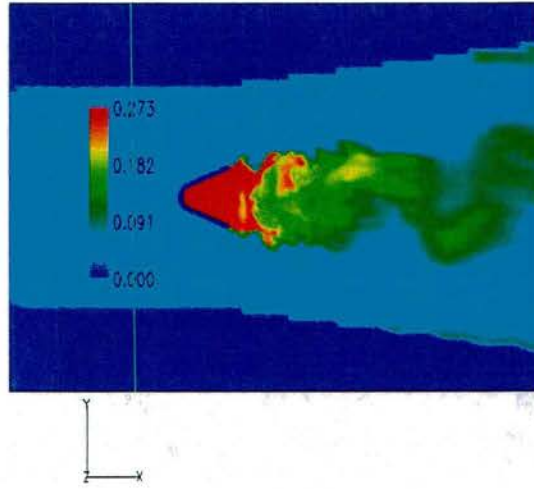


Figure 24: Progress variable at plane  $Z = 0$ .

and has therefore almost no CO. However, in the region downstream of this, the finite reaction progress is evident from the high CO concentrations. Figure 21 shows a comparison of the mean axial velocities along the centerline from the non-reactive and the reactive simulations. Both velocity profiles are very similar up to the end of the V-gutter. After that the reactive flow is accelerated by the heat release.

**CharLES Low Mach Formulation Cold Flow Results** - The large eddy simulation (LES) code, CharLES has been used to generate cold flow results for the AFRL flame holder geometry. An unstructured, hexahedral mesh of 5.9 million cells is used for the simulation. Figure 25 shows the computation domain. The underlying mesh is shown in Figs. 26, 27, and 28. Figures 29 and 30 show the mesh at the  $Z = 0$  midplane. Figures 31, 32, and 33 show contour plots of instantaneous axial velocity, time averaged axial velocity, and instantaneous vorticity magnitude in the  $Z = 0$  midplane. Figure 35 shows the vertical profiles ( $y$  direction) of the time averaged axial velocity at  $X=0.01\text{m}$  (right after the V-gutter),  $0.1\text{m}$  and  $0.7\text{m}$  in the  $Z=0$  midplane, the exact location being shown in Fig. 34. It clearly shows the formation of the wake in the region downstream of the V-gutter. Further downstream, the profile becomes more uniform.

**2D Unsteady RANS Cold Flow Results** - A leading commercial CFD code was used to solve the problem using an unsteady RANS approach in 2 dimensions. An unstructured, hexahedral mesh of around 255,000 cells, shown in figures 36, 37, and 38 was used. Figures 39 and 40 show the instantaneous and the time averaged axial velocity, while Fig. 41 shows the instantaneous vorticity magnitude. These results show coherent structures as the vortices are shed behind the V-gutter. This obviously is the incorrect solution in the considered regime.



Figure 25: Computational domain for CharLES simulation

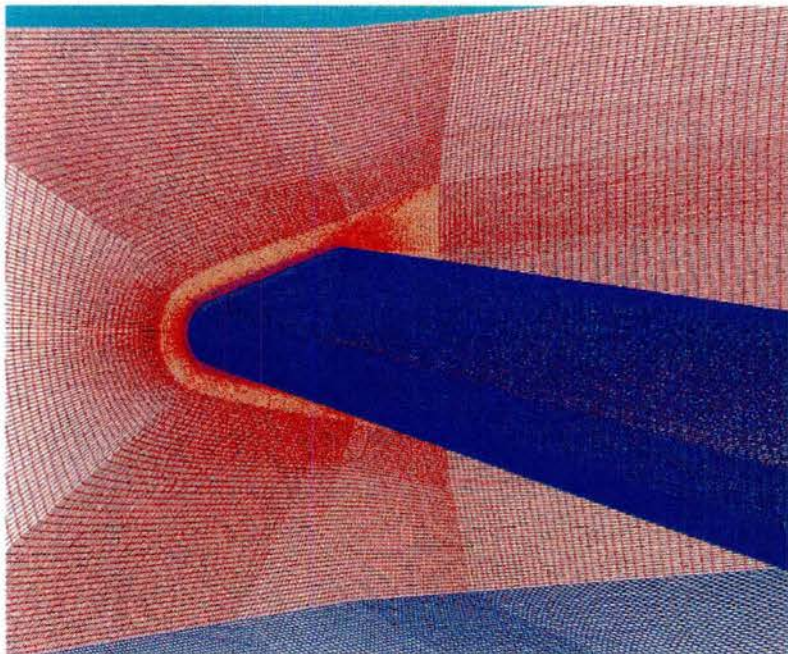


Figure 26: Computational mesh for CharLES simulation

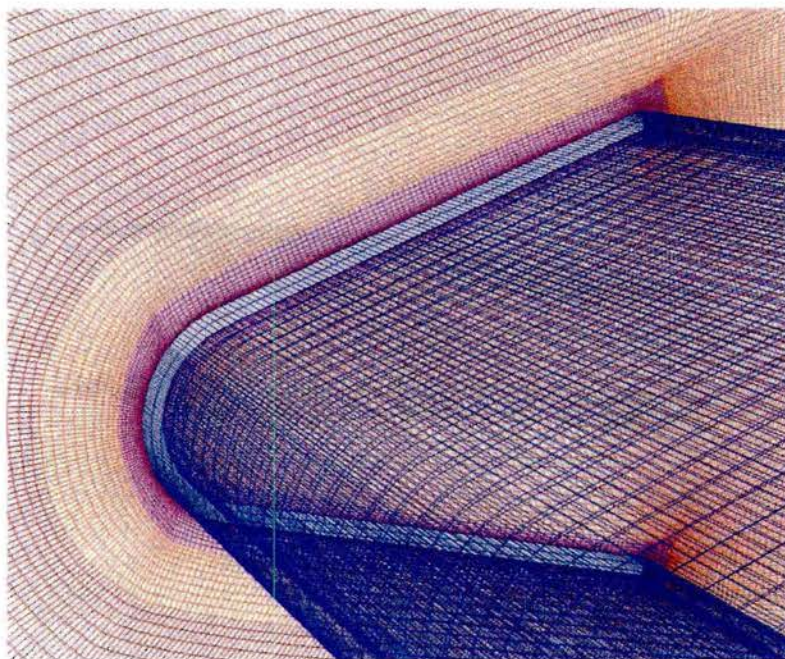


Figure 27: Computational mesh for CharLES simulation (magnified view)

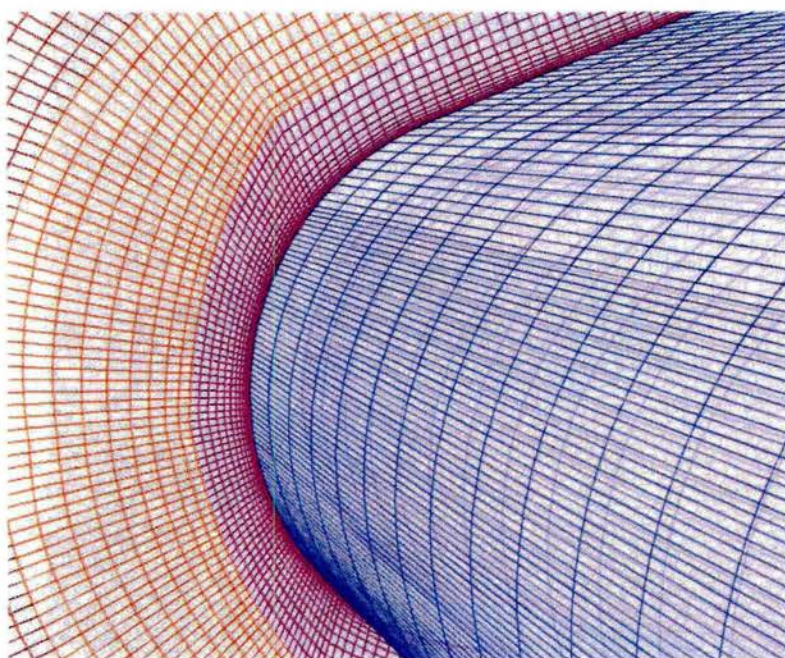


Figure 28: Computational mesh near the leading edge for CharLES simulation

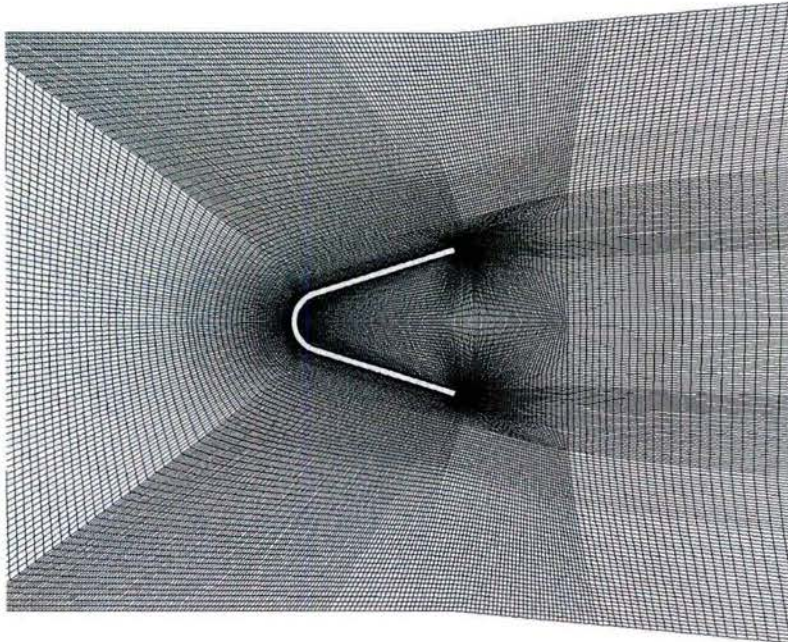


Figure 29: Computational mesh at the  $Z = 0$  plane for CharLES simulation

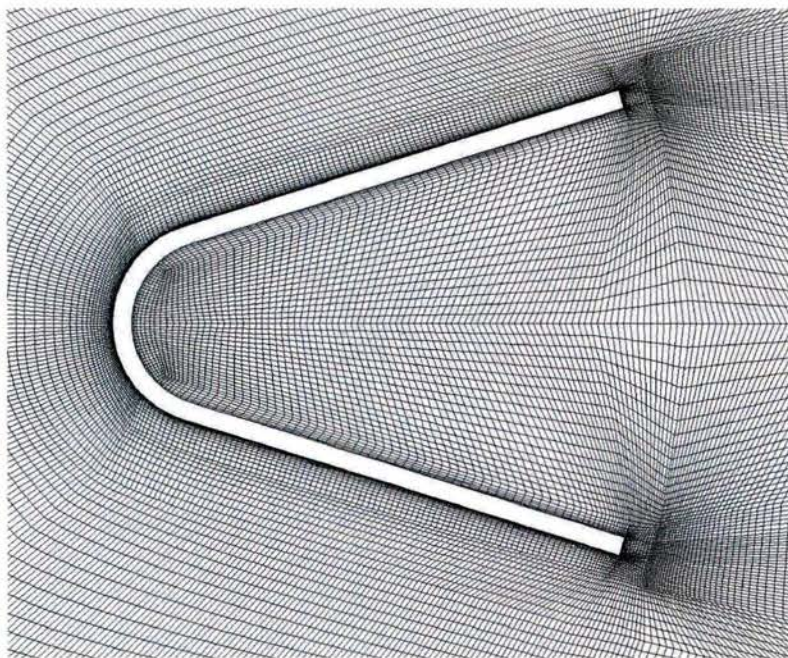


Figure 30: Computational mesh at the  $Z = 0$  plane for CharLES simulation (magnified view)

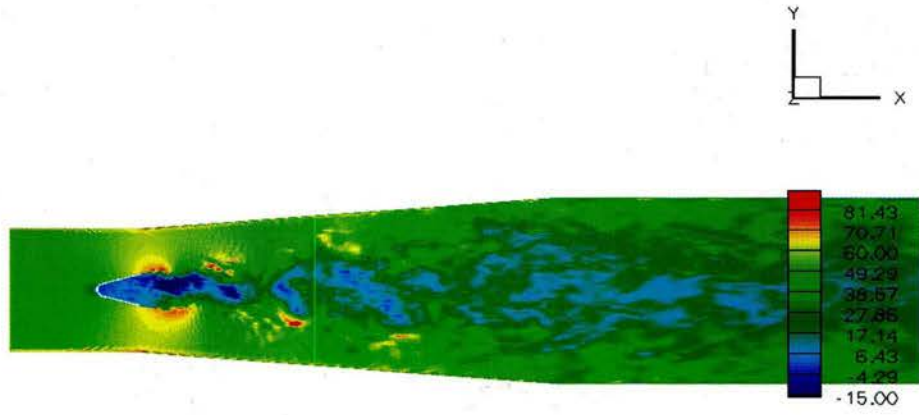


Figure 31: Instantaneous snapshot of the axial velocity component (m/s) at the  $Z = 0.0$  plane from CharLES simulation

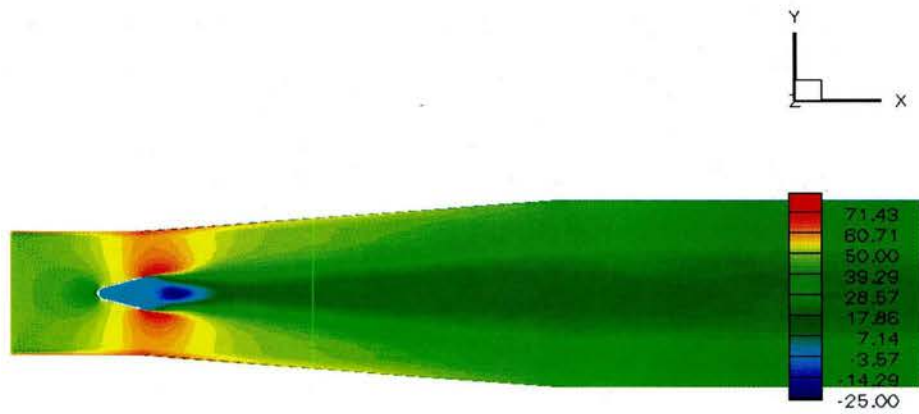


Figure 32: Time averaged axial velocity component (m/s) at the  $Z = 0.0$  plane from CharLES simulation

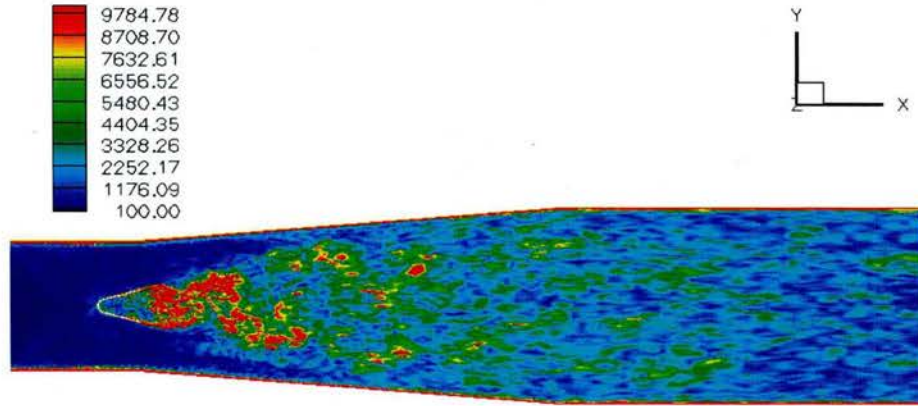


Figure 33: Instantaneous snapshot of vorticity magnitude (1/s) at  $Z = 0.0$  plane from CharLES simulation

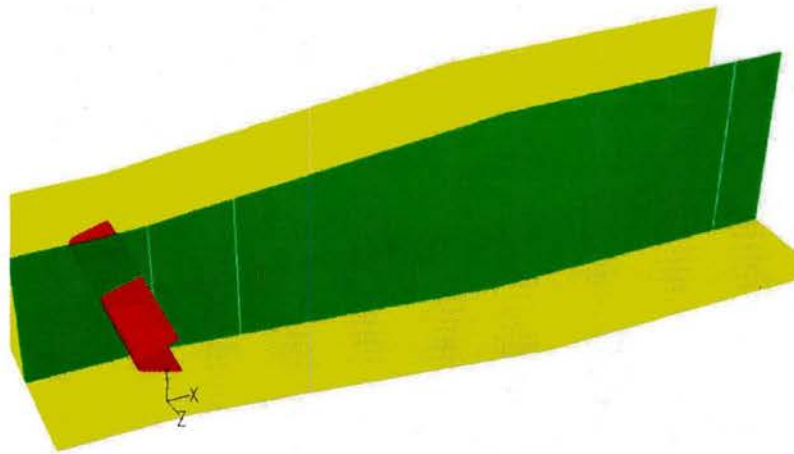


Figure 34: Location of the  $X=0.01\text{m}$ ,  $0.1\text{m}$  and  $0.7\text{m}$  lines in the  $Z = 0$  plane

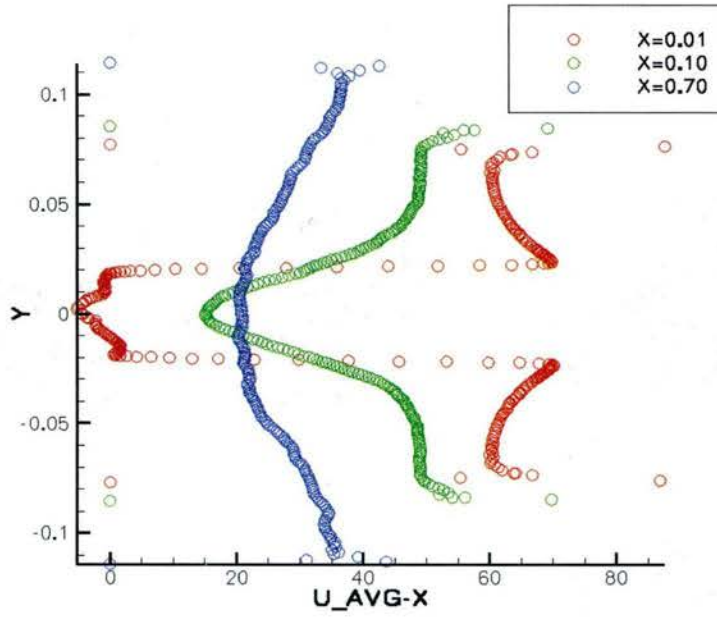


Figure 35: Profiles of time averaged axial velocity component (m/s) at  $X=0.01\text{m}$ ,  $0.1\text{m}$  and  $0.7\text{m}$  in  $Z = 0$  plane

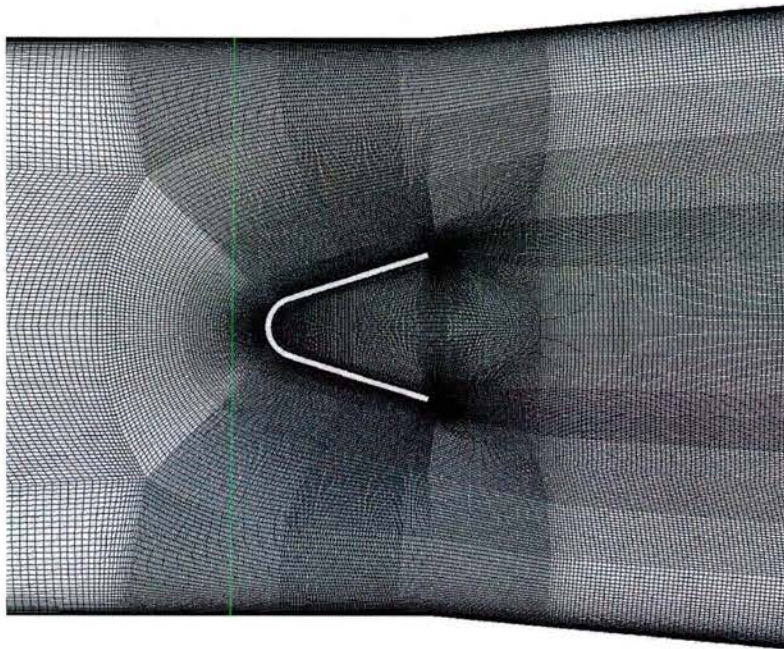


Figure 36: Computational mesh for 2D unsteady RANS simulation

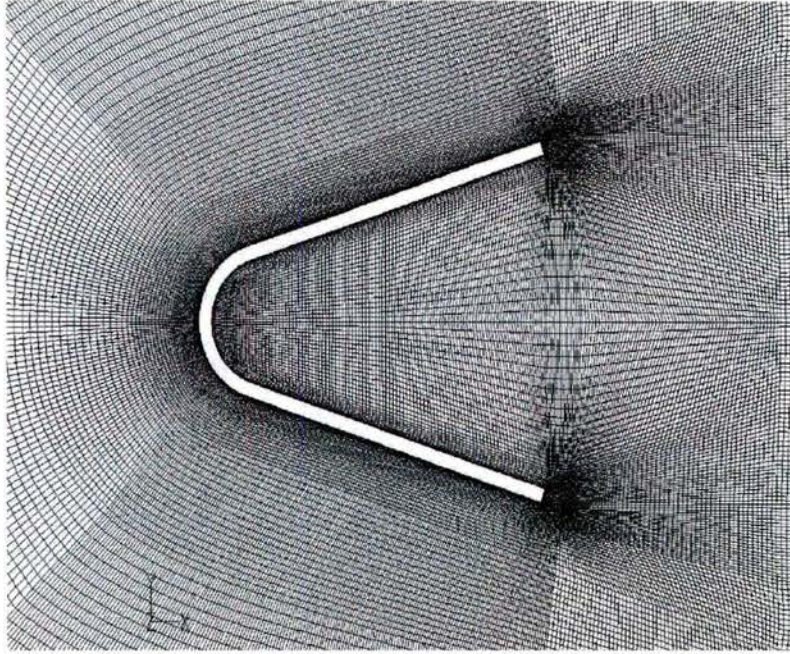


Figure 37: Computational mesh for 2D unsteady RANS simulation (magnified view)

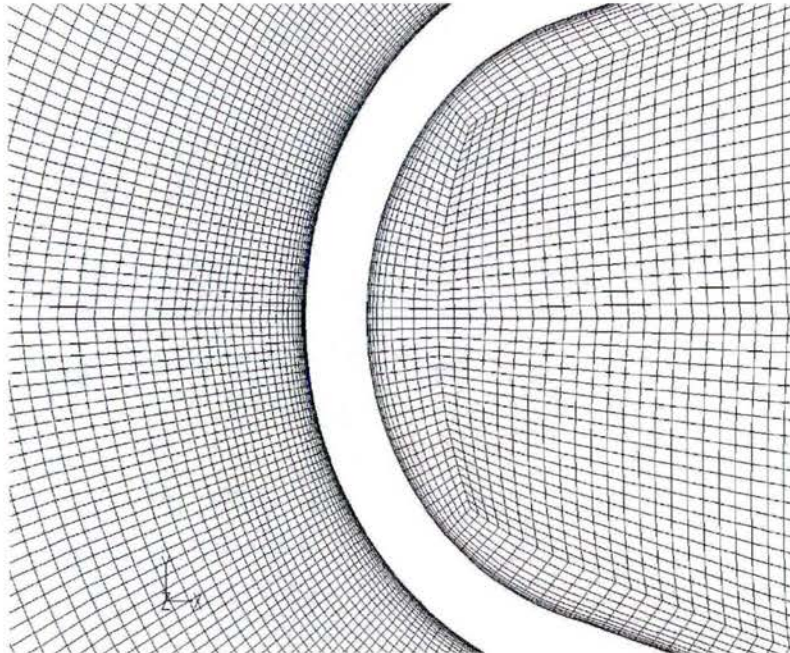


Figure 38: Computational mesh near the leading edge for 2D unsteady RANS simulation

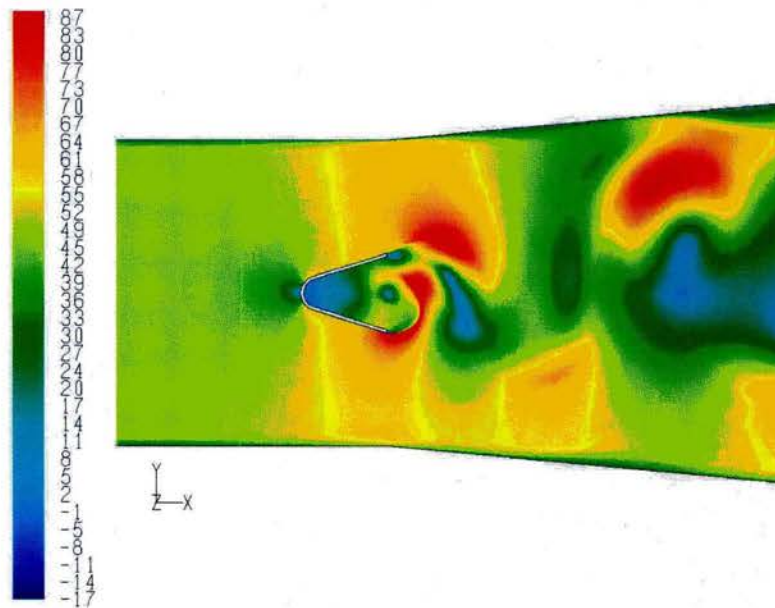


Figure 39: Instantaneous axial velocity (m/s) for 2D unsteady RANS simulation

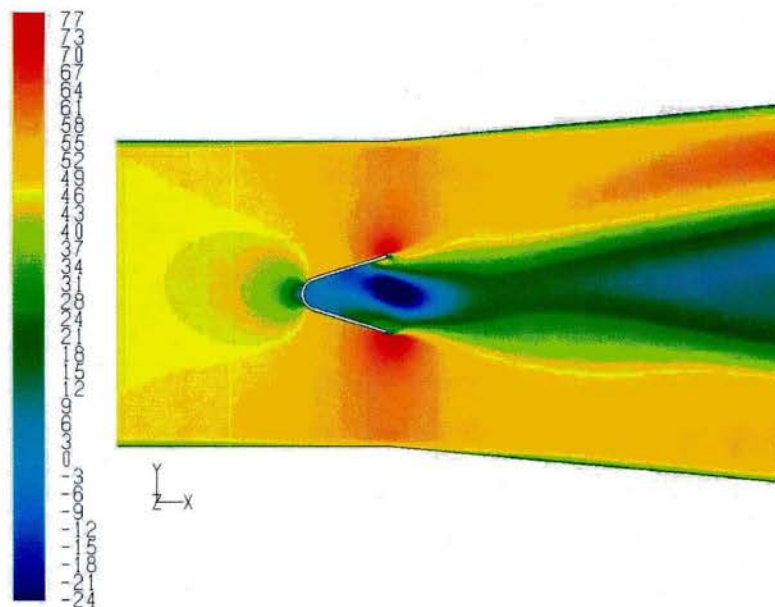


Figure 40: Time averaged axial velocity (m/s) for 2D unsteady RANS simulation

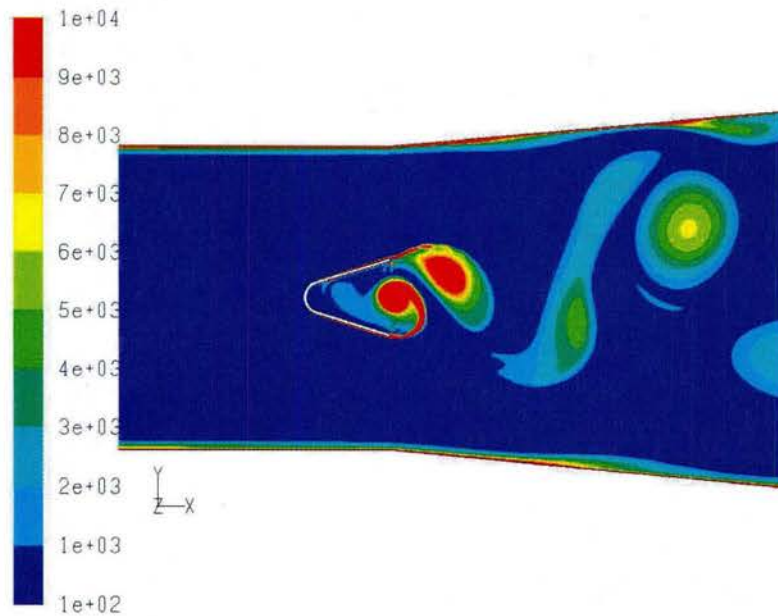


Figure 41: Instantaneous vorticity magnitude (1/s) for 2D unsteady RANS simulation

## 5 Personnel supported

Dr. Shoreh Hajiloo and Dr. Heinz Pitsch from CASCADE Technologies, Inc. and Prof. Godfrey Mungal and Dr. Wookyoung Kim from Stanford University were supported from this project.

## 6 Publications

1. H. El-Asrag, H. Pitsch, W. Kim, H. Do & M. G. Mungal (2008), "A Computational and Experimental Assessment of the Damkhler Number Similarity for Static Flame Stability in Augmentor Flows," *AIAA 2008-4955, 44th AIAA/ASME/SAE/ASEE Joint Propulsion Conference & Exhibit*, 21 - 23 July 2008, Hartford, CT.
2. Wookyoung Kim, Hyungrok Do, M. G. Mungal & M. A. Cappelli (2008), "Plasma Assisted Diffusion Flames: Role of Elevated Ambient Temperatures," to appear *IEEE Transactions on Plasma Science*.

## 7 Interactions/Transitions

1. M. G. Mungal (2008), "Jet Diffusion Flame Stabilization via Pulsed Plasma Forcing," Invited Keynote Lecture, *61<sup>st</sup> Gaseous Electronics Conference*, Oct 13-17, 2008, Dallas, TX.

2. High temperature plasma flame stabilization findings transferred to AFOSR MURI effort: "Experimental/Computational Studies of Combined/Cycle Propulsion: Physics and Transient Phenomena in Inlets and Scramjet Combustors."

## 8 New discoveries, inventions, or patent disclosures

None.

## 9 Honors/Awards

None.

## References

- [1] E. E. Zukowski and F. E. Marble. The role of wake transition in the process of flame stabilization on bluff-bodies. In *ARGAD Combustion Researches and Reviews*, pages 167–180. Butterworth Scientific Publishers, London, 1955.
- [2] J. P. Longwell, E. E. Forest, and M. A. Weiss. Flame stability in bluff-body recirculation zones. *Journal of Industrial and Engineering Chemistry*, 45:1629–1633, 1953.
- [3] C. R. King and S. Nakanishi. Effects of some configuration changes on afterburner combustion performance. *NACA Report, NACA-RM-E57C01*, 1957.
- [4] Y. Morinishi, O. V. Lund, O. V. Vasilyev, and P. Moin. Fully conservative higher order finite difference schemes for compressible flow. *Journal of Computational Physics*, 143:90 – 124, 1998.
- [5] O. Desjardins, G. Blanquart, G. Balarac, and H. Pitsch. High order conservative finite difference scheme for variable density low mach number turbulent flows. *Journal of Computational Physics*, in-press, 2008.
- [6] C. D. Pierce and P. Moin. *Progress-variable approach for large-eddy simulation of turbulent combustion*. Mechanical Engineering Department Report, TF-80, Stanford University, 2001.
- [7] P. Moin, K. Squires, W. Cabot, and S. Lee. A dynamic subgrid-scale model for compressible turbulence and scalar transport. *Physics of Fluid A*, 3:2746–2757, 1991.
- [8] A. W. Cook and J. R. James. Direct numerical simulation of a turbulent reactive plume on a parallel computer. *Journal of Computational Physics*, 129:263–283, 1996.

- [9] C. D. Pierce and P. Moin. Progress-variable approach for large-eddy simulation of non-premixed turbulent combustion. *Journal of Fluid Mechanics*, 504:73–97, 2004.
- [10] N. Peters. Laminar diffusion flamelet models in non-premixed turbulent combustion. *Progress of Energy and Combustion Science*, 10:319–339, 1984.
- [11] H. Pitsch. Large eddy simulation of turbulent combustion. *Annual Review of Fluid Mechanics*, 38:453 – 482, 2006.
- [12] M. Ihme, C. M. Cha, and H. Pitsch. Prediction of local extinction and re-ignition effects in non-premixed turbulent combustion using a flamelet/progress variable approach. *Proceedings of the Combustion Institute*, 30:793–800, 2005.
- [13] N. Peters. *Turbulent Combustion*. Cambridge University Press, 2006.
- [14] C. D. Pierce and P. Moin. A dynamic model for subgrid-scale variance and dissipation rate of a conserved scalar simulation of non-premixed turbulent combustion. *Physics of Fluids*, 10:3041–3044, 1998.
- [15] H. Pitsch and M. Ihme. An unsteady/flamelet progress variable method for les of non-premixed turbulent combustion. In *43<sup>rd</sup> AIAA Sciences Meeting and Exhibit, 10-13 Jan 2005, Reno, NV, AIAA 2005-0043*.
- [16] H. Pitsch and S. Fedotov. Investigation of scalar dissipation rate fluctuations in non-premixed turbulent combustion using a stochastic approach. *Combustion Theory and Modelling*, 5:41–57, 2001.
- [17] E. Knudsen and H. Pitsch. A general flamelet transformation useful for distinguishing between premixed and non-premixed modes of combustion. *Comb. Flame*, 2009. in press.